Geophysical Journal International

Geophys. J. Int. (2023) **235,** 2846–2861
Advance Access publication 2023 October 6
GJI Seismology

https://doi.org/10.1093/gji/ggad390

Inferring damage state and evolution with increasing stress using direct and coda wave velocity measurements in faulted and intact granite samples

Kiran Pandey,[1] Taka'aki Taira,[2] Georg Dresen[3] and Thomas H. Goebel[1]

[1]*Center for Earthquake Research and Information, University of Memphis, Memphis, TN 38152, USA. E-mail: kpandey@memphis.edu*
[2]*Berkeley Seismological Laboratory, University of California, Berkeley, CA 94720, USA*
[3]*Helmholtz Centre Potsdam, German Research Centre for Geosciences GFZ, 14473 Potsdam, Germany*

Accepted 2023 September 28. Received 2023 August 22; in original form 2023 February 28

SUMMARY

A better understanding of damage accumulation before dynamic failure events in geological material is essential to improve seismic hazard assessment. Previous research has demonstrated the sensitivity of seismic velocities to variations in crack geometry, with established evidence indicating that initial crack closure induces rapid changes in velocity. Our study extends these findings by investigating velocity changes by applying coda wave interferometry (CWI). We use an array of 16 piezoceramic transducers to send and record ultrasonic pulses and to determine changes in seismic velocity on intact and faulted Westerly granite samples. Velocity changes are determined from CWI and direct phase arrivals. This study consists of three sets of experiments designed to characterize variations in seismic velocity under various initial and boundary conditions. The first set of experiments tracks velocity changes during hydrostatic compression from 2 and 191 MPa in intact Westerly granite samples. The second set of experiments focuses on saw-cut samples with different roughness and examines the effects of confining pressure increase from 2 to 120 MPa. The dynamic formation of a fracture and the preceding damage accumulation is the focus of the third type of experiment, during which we fractured an initially intact rock sample by increasing the differential stress up to 780 MPa while keeping the sample confined at 75 MPa. The tests show that: (i) The velocity change for rough saw cut samples suggests that the changes in bulk material properties have a more pronounced influence than fault surface apertures or roughness. (ii) Seismic velocities demonstrate higher sensitivity to damage accumulation under increasing differential stress than macroscopic measurements. Axial stress measured by an external load cell deviates from linearity around two-third through the experiment at a stress level of 290 MPa higher than during the initial drop in seismic velocities. (iii) Direct waves exhibit strong anisotropy with increasing differential stress and accumulating damage before rock fracture. Coda waves, on the other hand, effectively average over elastic wave propagation for both fast and slow directions, and the resulting velocity estimates show little evidence for anisotropy. The results demonstrate the sensitivity of seismic velocity to damage evolution at various boundary conditions and progressive microcrack generation with long lead times before dynamic fracture.

Key words: Acoustic properties; Coda waves; Seismic anisotropy; Seismic velocity; Micromechanics of damage evolution.

1 INTRODUCTION

Dynamic failure events in earth material, such as rock bursts, landslides and earthquakes, are thought to be preceded by preparatory processes at different spatiotemporal scales. Such preparatory processes are characterized by subtle changes in frictional and elastic properties of geological material during stress accumulation. Theoretical and laboratory results highlight that earthquakes start gradually and gain momentum quickly before they emit seismic waves (Dieterich 1972, 1978; Ohnaka 1992; Marone 1998; Ohnaka & Shen 1999; McLaskey & Kilgore 2013; Latour *et al.* 2013; Passelègue *et al.* 2018; McLaskey 2019). This nucleation phase marks the onset of shear rupture propagation (Dieterich 1978; Ohnaka 1992, 2004; McLaskey & Kilgore 2013; Latour *et al.* 2013). Before

rupture propagation, microcrack damage progressively localizes along the future nucleation zone, eventually promoting frictional failure (Lockner *et al.* 1991; Ohnaka 1992, 2004; Guérin-Marthe *et al.* 2019; Dresen *et al.* 2020). Since many aspects of laboratory friction experiments are highly idealized compared to natural faults (Goebel *et al.* 2015), it is not always straightforward that results from laboratory-sized samples can yield knowledge significant to earthquake faulting (Marone 1998; Ohnaka 2004).

Despite obvious differences between faults in the lab and in nature, experimental results significantly improved our understanding of the physical mechanisms behind slip localization and dynamic instability. Specific phases of pre-failure damage accumulation and coalescence characterize intact rock failure in the laboratory. A nucleation patch forms when microcracks start to localize spatially, interact and coalesce (Scholz 1968; Lockner *et al.* 1991; Main *et al.* 1992; Ohnaka 1992, 2004). Micromechanical models are used to quantify damage accumulation and macroscopic failure (Ashby & Hallam 1986; Ashby & Sammis 1990; Kachanov 1994; Bhat *et al.* 2011), for instance, in a porous brittle medium under uniaxial compression (Ashby & Hallam 1986). Crack growth in this 'pore-crack' model occurs in the direction of maximum principal stress when stress intensity at the crack tip exceeds the fracture toughness (Ashby & Hallam 1986). To comprehend the mechanism of fracture formation and propagation in less permeable brittle rock, Ashby & Sammis (1990) suggested a 'wing-crack' model. In such a model, cracks form at an angle between 30° and 60° to the maximum principal stress (Ashby & Hallam 1986). When the shear crack overcomes the frictional resistance, it will slide and promote the formation of wing cracks at its tips (Ashby & Sammis 1990). In these models, as the loading increases, the microcracks interact to create a fault nucleus that precedes failure analogous to laboratory observations. Damage accumulation and preparatory processes before failure in numerical models and laboratory experiments are also considered important processes that govern fault mechanics in the natural system (Ben-zion & Sammis 2003). However, potential precursory signals are often absent or hard to detect in field observation (Ellsworth 2019; Tape *et al.* 2013).

Laboratory fracture and frictional sliding tests have produced much insight into the constitutive behaviour of fault zones. Seismic records during these tests show several parallels to natural seismicity (Goebel *et al.* 2012, 2013; Acosta *et al.* 2019; Marty *et al.* 2023). For instance, several studies suggest frequent foreshock activity can be detected in areas with high-density seismic instrumentation (Mignan 2014; Sugan *et al.* 2014; Trugman & Ross 2019). This observation may be similar to abundantly recorded foreshocks in experiments with high-resolution acoustic emission monitoring (Goebel *et al.* 2012; Johnson *et al.* 2013; Rouet-Leduc *et al.* 2017; Dresen *et al.* 2020; Trugman *et al.* 2020; Aben *et al.* 2020; Johnson *et al.* 2021; Marty *et al.* 2023).

One issue that hampers a more robust foreshock analysis is the need for high-resolution records of very low-magnitude earthquakes in nature. Seismic velocity—which records the change in the fault zone and elastic bulk properties—is another extensively used measure of the accumulation and evolution of damage along a fault with increasing differential stress. The usefulness of this method has been tested in monitoring volcanic processes (Ratdomopurbo & Poupinet 1995; Brenguier *et al.* 2008b; Feng *et al.* 2020), near-surface damage induced by earthquakes (Vidale & Li 2003; Wegler *et al.* 2009; Taira *et al.* 2015; Wang *et al.* 2019; Taylor & Hillers 2020) and laboratory faults (Scuderi *et al.* 2016; Bolton *et al.* 2020; Paglialunga *et al.* 2021; Shreedharan *et al.* 2021).

Variations in seismic velocities are frequently inferred from inverting direct *P* and *S* phase picks, for example in tomographic studies (Aki & Lee 1976; Husen & Kissling 2001; Thurber & Ritsema 2007; Islam *et al.* 2022). The fundamental data utilized are the arrival times of the *P* and *S* phases. The method for tomographic inversion has evolved from simple 3-D tomographic inversion (Diehl *et al.* 2009; Barklage *et al.* 2015; Brantut 2018) to more complex double-difference tomography (Zhang & Thurber 2003). Similarly, waveform inversion techniques using body and surface waves are used to determine the velocity structure of the earth at different depths (Tape *et al.* 2009; Adourian *et al.* 2022). In all these techniques, fundamental data utilized are the absolute traveltime or differential traveltime of the P and S phases, which are accompanied by uncertainties in their pick times and event locations. In addition to that, the path or region traversed by the respective phases is sampled just once.

Coda wave interferometry (CWI) methods take advantage of multiply scattered waves that sample volumetric velocity changes more extensively and are thus thought to have higher sensitivity than direct phase measurements (Snieder *et al.* 2002; Grêt 2003; Grêt *et al.* 2006; Snieder 2006). CWI is based on the principle that a coda wave samples many scatterers formed during varying boundary conditions (Grêt *et al.* 2006; Snieder 2006). The wave will bounce multiple times from the scatterer (Singh *et al.* 2019) in such a case. Slight changes in a medium that may not appear in the first arrivals are amplified by this repeated sampling (Grêt *et al.* 2006); however, anisotropy-effects on CWI-velocity are largely unknown and are investigated in the following.

CWI does not require information on source and receiver location to estimate the velocity change beyond the identification of highly correlated waveforms. The source could be either an active wave generator (e.g. piezo transducers, vibroseis trucks, or explosion) or a passive source such as repeating earthquakes. Repeating earthquakes are seismic events with identical locations and geometry but occur at distinct times (Uchida & Bürgmann 2019).

CWI has been used to detect temporal changes in the stress state in the seismogenic crust (Brenguier *et al.* 2008a; Wegler *et al.* 2009). CWI is also associated with detecting seismogenic stress evolution along the San Andreas Fault after the 2004 Parkfield earthquake (Taira *et al.* 2008), associated with the three scatterers located on the fault at the rupture's northernmost extent. Similarly, CWI is used to monitor the reservoir response to earthquakes in the Salton Sea geothermal field (Taira *et al.* 2018). As a result of aseismic deformation, the opening of fractures was responsible for the observed decrease in velocity. Likewise, prior to the eruption of the Kilauea volcano in December 2017, noise-based interferometry indicated three phases of the evolution and interaction of the reservoir-dike magmatic system (Feng *et al.* 2020). Detailed velocity measurements in volcanic environments may help document pre-eruptive processes and image magma systems.

CWI methods are also used to monitor the time-varying rock properties in the laboratory (Grêt *et al.* 2006). Grêt *et al.* (2006) determined the dependence of velocity on uniaxial stress resulting from temperature and water saturation. In addition to its usefulness in studying geological material, CWI has also found widespread usage in monitoring the growth of microcracks and the strength of concrete in civil engineering (Garnier *et al.* 2013; Livings *et al.* 2016; Jiang *et al.* 2020). The significance of the method can be inferred from its multiple applications, which have proved its usefulness in a wide range of settings and materials.

In the following sections, we look at how changes in seismic velocity can be measured during differential stress increase leading up to dynamic failure and confining pressure increase during hydrostatic loading of intact and faulted samples. We start by summarizing the CWI methodology and the data used in this study. The

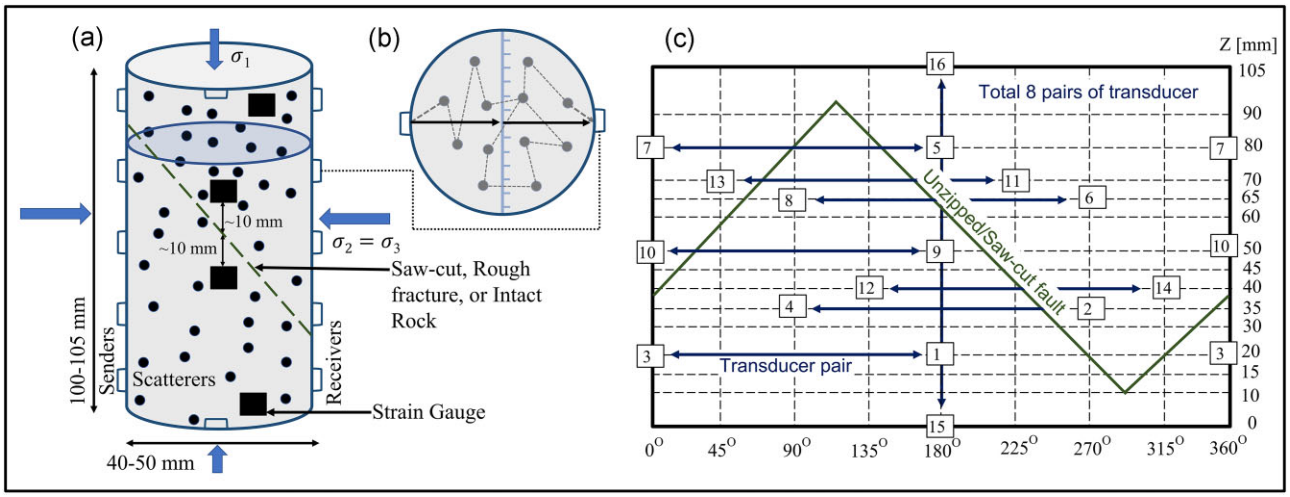

Figure 1. (a) Schematic diagram representing the state of stress (σ_1, σ_2 and σ_3 represent the largest compressive stress, intermediate stress, and least principal stress, respectively), saw-cut fault (blue dashed line) for faulted sample, and scatterers in the rock sample. Sample lengths varied between 100 and 105 mm, and diameter was either 40 or 50 mm. In an active source experiment with sender and receiver pairs, the piezoceramic transducers were directly attached to the rock surface through the rubber jacket. On the sample were two sets of strain gauges, one running circumferentially and the other running axially (black square box). (b) Plan-sectional view of the rock cylinder along its diameter. The solid black lines denote the direct ray path, and the dashed black lines represent the multiply scattered elastic waves from the sender towards the receiver during an experiment. (c) Location of sensors on the rock sample during the experiment and mapping for saw-cut and fractured samples in green. A total of 16 transducers were used, with seven transducer pairs in horizontal alignment and one pair in a vertical arrangement.

described methodology is then evaluated on synthetic data sets to compare the robustness and resolution of the two different CWI implementations, that is a moving windowed cross-correlation (MWC) approach (Snieder *et al.* 2002; Grêt *et al.* 2006; Snieder 2006) and dynamic time warping (DTW; Sakoe & Chiba 1978; Hale 2013; Mikesell *et al.* 2015). In the third step, we use CWI to derive velocity changes during (i) intact rock compression, (ii) hydrostatic compression of saw-cuts with different roughness and (iii) triaxial loading to intact rock failure.

2 EXPERIMENTAL SETUP, DATA AND METHODS

2.1 Laboratory experimentation

This study focuses on seismic velocity changes with increasing confining pressures and axial load before rock fracture in cylindrical Westerly granite samples (40–50 mm in diameter and 105 mm in height). The samples are comprised of quartz (28 per cent), plagioclase feldspar (33 per cent), orthoclase feldspar (33 per cent) and mica (5 per cent), including muscovite and biotite (Chayes 1950). The grain size of minerals in the granite sample ranges from 0.05 to 2.2 mm, with an average grain size of 0.75 mm (Stesky, 1978). The initial porosity of the sample was less than 2 per cent (Goebel *et al.* 2012). The selected samples were checked for homogeneity and showed no macroscopic evidence of fracturing or inclusions. The samples were oven dried for several days to remove the moisture content and then placed inside a rubber jacket to separate rock-sample and confining oil.

The deformation and microcrack formation in the sample was thoroughly monitored by an array of piezoceramic transducers (Fig. 1c). The transducers were mounted directly on the rock samples through holes in the rubber jackets using low-viscosity epoxy. We utilized 16 different piezoceramic sensors with a thickness of 1 mm (for samples with a diameter of 40 mm) or 2 mm (for samples with a diameter of 50 mm) and a resonance frequency of 1–2 MHz for acoustic emission recording and ultrasonic pulse generation. The experiments focused on active source velocity measurements, with one transducer (sender) sending an ultrasonic pulse (duration = 3.63 μs) every 30 s and the other transducers (receiver) receiving the signal that propagated through the sample (Stanchits *et al.* 2006; Goebel *et al.* 2013). The 16-channel array was designed to include seven horizontal and one vertical sensor pair (Fig. 1c). Vertical velocity measurements were obtained from AE sensors that were directly embedded in the vertical loading pistons. Each channel operates in a triggered mode and records full waveforms at a sampling rate of 10 MHz with a time resolution of 0.1 μs and an amplitude resolution of 16 bits (Goebel *et al.* 2012). The 16-bit amplitude resolution refers to the accuracy of the piezoceramic transducer, which can detect small changes in amplitude. The higher bit resolution allows for a larger set of potential amplitude values, allowing for an accurate and detailed representation of the input signal.

The experiments were performed on a 4600 kN MTS servo-controlled loading frame, and a 200 MPa pressure vessel system at the German Research Centre for Geosciences (GFZ)-Potsdam, Germany. Internal and external load cells were used to measure the axial load, and a Linear Variable Displacement Transducer (LVDT) was used to monitor axial displacement and shortening across the whole sample. Two pairs of strain gauges were arranged axially and circumferentially on the sample surface for the experiments. The circumferential strain gauges were directly attached to the sample surface at 10 mm below and above the saw-cut fault.

We conducted three experiments to investigate the relationship between changes in seismic velocity (i.e. direct *P* wave and coda wave), fault damage, and stress state, each with different loading conditions (Table 1). The first set of experiments explored the effect of changes in confining pressure (Fig. 1a) on microcracks and seismic velocities sampled in 30 s intervals. We increased the confining

Table 1. Summary of experiments conducted under varying levels of stress (S. no., serial number). Int-1 and Int-2 are two experiments involving the compression of intact rocks by hydrostatically increasing confining pressure. The second type of experiment was conducted on rough (FaultR) and smooth (FaultS) saw-cut samples, which were also subjected to an increase in confining pressure. Frac-1 is an experiment in which an intact rock is subjected to differential loading until failure.

S. no.	Sample ID	P_c (or σ_1–σ_3) - start (MPa)	P_c (or σ_1–σ_3) - end (MPa)	Pressure or piston loading rate	Diameter (mm)	Sample type
1	Int-1	2	75	0.5 MPa min^{-1}	40	Intact
2	Int-2	2	191 - 75[a]	0.5 MPa min^{-1}	40	Intact
3	FaultR-1	2	120	2.0 MPa min^{-1}	50	Faulted
4	FaultR-2	2	120	2.0 MPa min^{-1}	50	Faulted
5	FaultR-3	75	120	2.0 MPa min^{-1}	40	Faulted
5	FaultS-1	2	120	2.0 MPa min^{-1}	50	Faulted
6	FaultS-2	2	120	2.0 MPa min^{-1}	50	Faulted
7	Frac-1	0	784[b]	20 μ min^{-1}	40	Intact

[a]Int-2 is the case where confining pressure was increased to 191 MPa from 2 MPa and then decreased back to 75 MPa.
[b]Experiment Frac-1 is where the differential stress (confining pressure fixed at 75 MPa) was increased until the sample failed, where axial loading rate is 20 μ/min.

pressures from 2 to 75 MPa (Int-1) and from 2 to 191 MPa and back down to 75 MPa (Int-2) at 0.5 MPa/min to explore crack closure and reopening.

The second set of experiments focused on velocity changes on smooth and rough saw-cut faults oriented at a 30° angle to the loading axis (Fig. 1a). The smooth and rough surfaces were created by cutting the samples at a 30° angle to the vertical axis. The resulting surface was then ground using two different silicon-carbide powders (#290 for smooth/polished surface and #60 for rough surface) leading to RMS roughness of 0.01 mm (FaultS-1 and FaultS-2) and 0.15 mm (FaultR-1, FaultR-2 and FaultR-3; Table 1). In each experiment, the confining pressure was increased from 2 to 120 MPa at a rate of 2.0 MPa min^{-1}.

The third type of experiment focused on velocity changes before intact rock fracture (Frac-1). Here, a rock sample with 40 mm diameter and 100 mm length was placed in a triaxial apparatus, and the confining pressure was increased to 75 MPa and held constant. The axial load was then increased until the sample fractured, and a new fault formed. The locations and magnitudes of the associated acoustic emissions (AEs) were estimated using the methods discussed by Goebel *et al*. (2013).

2.2 Determination of the relative change in velocity

We started the computation by estimating the velocity of the *P* wave. By measuring the *P*-wave velocity change, normal and parallel to the sample axis, we can infer changes in material properties along the source– path. We were also interested in monitoring changes in velocity related to coda waves. Coda waves are thought to be the outcome of seismic wave scattering mechanisms generated by heterogeneities (Herraiz & Espinosa 1987). As a result, we assume that the coda waves sample a more extensive section of the rock in some instances (Grêt *et al.* 2006; Snieder 2006), and report changes that the direct *P* phase has missed. We use the moving window cross-correlation technique (MWC; Snieder *et al.* 2002; Grêt 2003; Zotz-Wilson *et al.* 2019; Singh *et al.* 2019) and the dynamic time warping method (DTW; Sakoe & Chiba 1978; Müller 2007; Mikesell *et al.* 2015) to calculate the time lag between two successive waves.

We aim to capture temporal variations in laboratory fault properties and how they evolve as failure approaches under different boundary conditions. Using controlled laboratory experiments with known geometry and boundary conditions, we determined whether and under what conditions CWI can provide more precise measurements of changes in seismic velocities and fault zone properties.

2.3 Direct *P*-wave velocity

During our experiment, the source generates a pulse of length 3.63 μs, and the receiver records the waves transmitted through the sample. The start of the source pulse at the sender is considered the origin time. We used the Akaike Information Criterion (AIC) technique (Akaike 1974; Kurz *et al.* 2005) to determine the arrival time of the direct *P* phase. We determined the relative change in *P*-wave velocity (dv_p/v_p) using these absolute times and sample geometry. The vertical velocity is adjusted to account for the shortening of the sample, as this contraction has a significant influence on the measured values. In contrast, the radial velocity, subject to a negligible change (see Suppl. 6), is considered insignificant and therefore left uncorrected.

2.4 Coda wave interferometry

We start by cross-correlating pairs of ultrasonic pulse (UP) source seismograms while pressure or stress increases. Let us assume a trace as u_{unp} (i.e. Event-114 in Fig. 2) at some time t under some state of stress. We then perturb the stress at time $t + dt$ and record another waveform trace u_{per} (i.e. Event-115 in Fig. 2). We extract the lag from the data using the cross-correlation function R, which is defined as,

$$R^{(t,T)}(t_s) \equiv \frac{\int_{t-T}^{t+T} u_{unp}(t')\, u_{per}(t' + t_s)\, dt'}{\left\{\int_{t-T}^{t+T} u_{unp}^2(t')\, dt' \int_{t-T}^{t+T} u_{per}^2(t')\, dt'\right\}^{1/2}}. \quad (1)$$

We compute the moving window cross-correlation between the two signals by eq. (1). The time window is centred at time t with a duration of $2T$ and the time-shift for the cross-correlation is denoted by t_s. Thus, the maximum time-shifted cross-correlation occurs when:

$$t_s = \langle\tau\rangle_{(t,T)}. \quad (2)$$

Here, $\langle\tau\rangle_{(t,T)}$ is the mean traveltime perturbation of the arrivals in the time window. The velocity of the medium is changed by a constant value δ_v when perturbing the state of stress (Snieder *et al.* 2002). We compute the mean traveltime perturbation as $\langle\tau\rangle_{(t,T)} = -(\frac{\delta v}{v})t$. Now, the estimated velocity change is:

$$\frac{\delta v}{v} = -\frac{\langle\tau\rangle_{(t,T)}}{t}. \quad (3)$$

We begin by examining the waveform coherency of the intact sample from active source experiments. Based on digital triggers

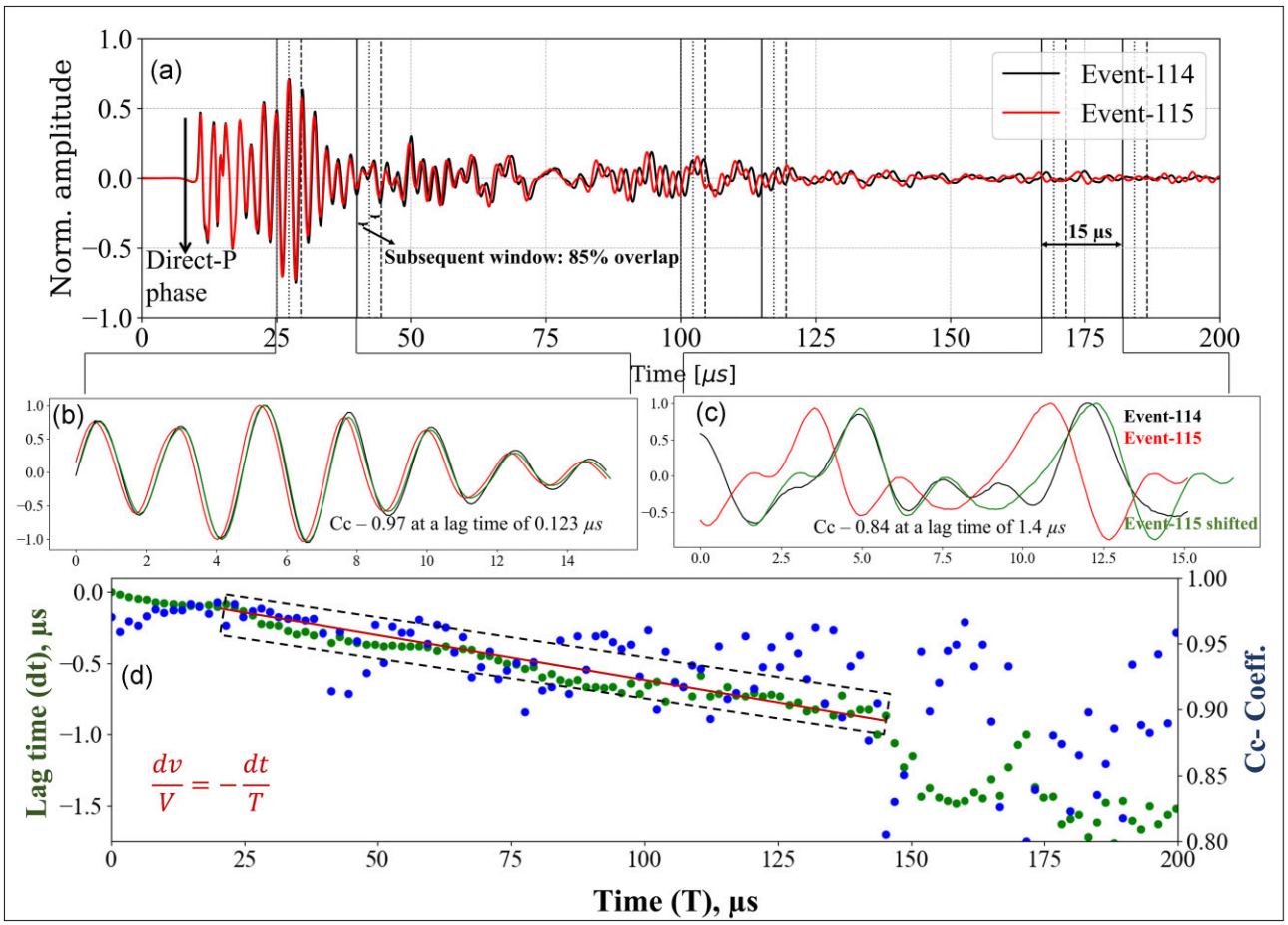

Figure 2. Two consecutive waveforms from a confining pressure increase experiment shows they are highly coherent. It also shows the 15 μs waveform window and an overlap of 85 per cent between two consecutive waveforms. The early part of the consecutive waveforms is highly coherent (b, c, d) with a very small lag. However, the later part has a very low cross-correlation value with a high associated lag. (d) Lag time over the length of the waveform shows the progression of the cross-correlation coefficient (blue) and the lag time (green) with the moving window cross-correlation method. The linear slope (ordinary least square fit) between 20 and 150 μs is considered for the dt/T, which is equivalent to $-$dv/V (Snieder *et al.* 2002).

sent directly from the pulse generator, these waveforms are recorded for 200 μs. The observed active source waveforms typically have a high signal-to-noise ratio for at least 150 μs with high cross-correlation values ($R > 0.9$). We consider the lag (dt) from 20 to 150 μs for the change in velocity estimates with the coda wave (saw-cut faulted samples and Frac-1). Based on these records, accurate time-shifts within the coda wave were determined by using the moving window cross-correlation method (Fig. 2). The relative velocity change that we are interested in is the overall slope of these discrete, windowed intervals (Fig. 2d; eq. 3). In this study, we utilized consecutive (alternate) waveforms throughout the experiment to calculate the CWI.

The following section discusses the DTW method which calculates the time-shift between individual samples of two waveforms by minimizing their Euclidean distance.

DTW is a non-linear optimization method that can resolve the time-shifts between the waveforms even in the presence of some random noise (Sakoe & Chiba 1978; Müller 2007; Mikesell *et al.* 2015). In this study, we assume a trace as $u_0(t)$ at some time t_1. We then change the state of stress at time t_2 and record another trace $u(t')$. In both cases, we only change the state of stress, and everything else was held constant, and the waveforms looked highly coherent [for example, $u_0(t)$ = Event-114 and $u(t')$ = Event-115 in Fig. 2]. There are several steps required to estimate the precise time-shift as discussed in Hale (2013).

First, compute the alignment error or error function between the two traces:

$$\text{i.e. } e[i,\tau] = \left(u(t') - u_0(t+\tau)\right)^2, \tag{4}$$

where τ is the lag given as an input. This error function returns a square matrix that has the same dimensions as the two traces. In the cells where τ is equal to the lag incurred due to the change in stress state, the error functions are close to zero.

The next step is to accumulate the error function with time, which is also called the distance function d(t,τ) (Mikesell *et al.* 2015):

$$d[0,\tau] = e[0,\tau],$$
$$d[i,\tau] = e[i,\tau] + \min\begin{Bmatrix} d[i-1,\tau-1], \\ d[i-1,\tau], \\ d[i-1,\tau+1] \end{Bmatrix}, \tag{5}$$
$$\text{for } i = 1, 2, \ldots, N-1.$$

In the first step, it is not always possible to locate the minimizing path (i.e. $u[0\colon N-1]$). Consequently, we must compute and store distances $d[i, l]$ for all lags, presuming that lag τ may lie on the

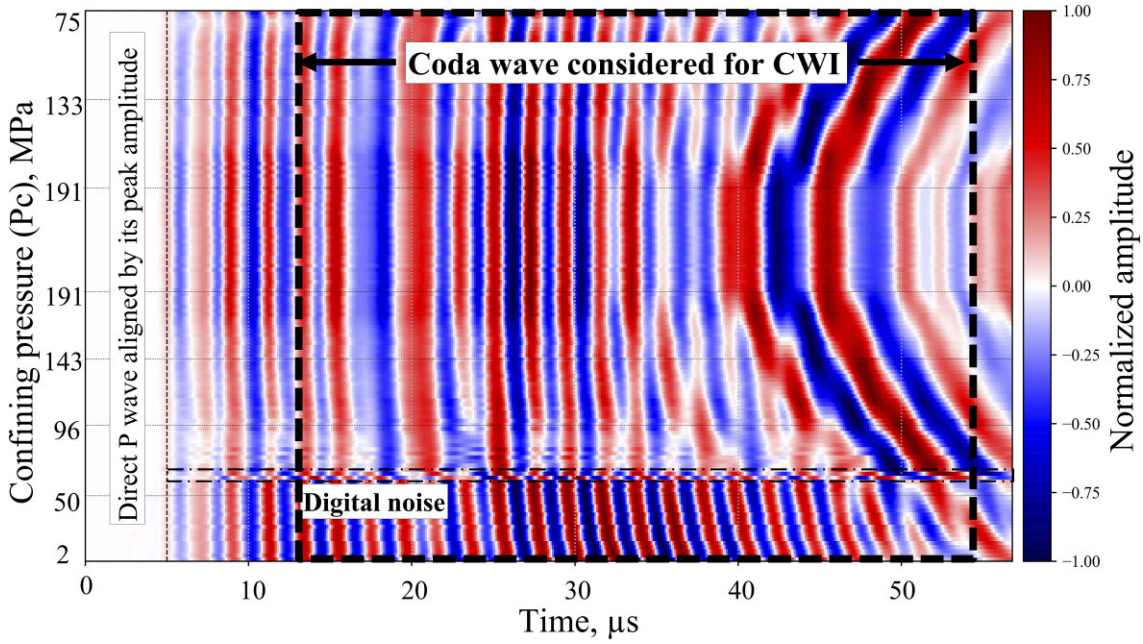

Figure 3. Confining pressure change versus the waveforms recorded during the Int-2 experiment for Sender-4 and Receiver-2 pair. All the waveforms were normalized by the maximum amplitude of the overall recorded waveforms. The *P* arrivals were used to align the normalized waveforms where the *P* phase was picked using the AIC picker. The confining pressure was increased from 2 to 191 MPa, then held constant at 191 MPa for 120 min and it lowered to 75 MPa. We observe some digital noise between 60 and 70 MPa, but the recordings are otherwise highly coherent. The red shades of colour represent the positive amplitude and the blue shades of color represent the negative amplitude. The black dashed box shows the length of the coda wave used for CWI.

minimizing path (Mikesell *et al.* 2015). Thus, eq. (5) will use the matrix computed in eq. (4) to compute the distance matrix d. By using this distance function, we can find the minimum accumulated distance D as:

$$D = \tau_{\min} d[N-1, \tau]. \tag{6}$$

This step loops over all the lags τ ($+\tau$ to $-\tau$) and finds the minimum distance over the matrix (Hale 2013). We select lags 'τ' ranging from -10 to $+10$ μs.

The third step is to find the minimizing path starting with the last shift from eq. (6), from matrix D. We backtrack through the D matrix (retracing the path with the lowest accumulated D from the bottom-left-hand corner to the top-right-hand corner) to find the optimal warping path, also known as the warping function (Hale 2013), or the actual lag incurred by the change in stress state during the experiment. The warping path serves as the mapping between the corresponding sampling points of the two traces. This is the last parameter needed to compute the relative change in velocity. This warping function is the absolute lag at each sample point across the pair of traces, as opposed to MWC, which is a relative lag dependent on the cross-correlation window size. The linear fit (dt/T) over this warping function will give us (dv/V) equivalent to eq. (3).

3 EXPERIMENTAL RESULTS

3.1 Increasing confining pressure on Intact rock

We hydrostatically compressed two intact granite samples (Int-1 and Int-2) in a triaxial loading rig by increasing the confining pressure from 2 to 75 MPa for the first and from 2 to 191 MPa and then back to 75 MPa for the second specimen (Table:1, Int-1) while keeping the rest of the boundary condition the same. The laboratory seismograms mirror the compression and stretching pattern of synthetic waveforms (see Suppl. 1 and 2) during confining pressure increase and decrease (Fig. 3). The lab waveforms were normalized by the highest maximum amplitude out of all records, and we aligned each trace at *P* onset, selected by an automatic AIC picker (Zhang & Thurber 2003; Kurz *et al.* 2005). For experiments Int-1 and Int-2, the waveforms were trimmed to 55 μs, and the MWC method's window length is 6 μs, with 85 per cent overlap (i.e. 5.1 μs). To identify the optimal window length and percent overlap, various combinations of window and overlap were tested on synthetic and experimental waveforms. The window parameters that yielded consistent and accurate results were then selected and fixed for further analysis using the MWC method.

We observe a strong correlation between confining pressure and coda wave characteristics. Confining pressure increase from 2 to 191 MPa leads to a clear compression of the waveforms (i.e. a decrease in lag time). A subsequent decrease in confining pressure from 191 to 75 MPa leads to systematic waveform stretching (i.e. an increase in lag), whereas waveforms remain roughly unchanged during constant confinement.

Using the *P* arrival times and the distance between the sender–receiver pair, we calculated the direct *P*-wave velocity for each waveform. The relative change in *P*-wave velocity throughout the experiment demonstrates an exponential increase during low confining pressures (Fig. 4). The total velocity change for a 2–191 MPa confining pressure increase is approximately 27.7 per cent, with 21.4 per cent associated with 2–44 MPa (Stage I) and the remaining 6.3 per cent associated with 44–191 MPa (Stage II in Fig. 4). The velocity was nearly constant (i.e. $\sim$ 27.7 per cent) for the period where confining pressure was held constant at 191 MPa (for 120 min). This indicates that the maximum change in the medium occurred during the initial confining pressure increase. The *P*-wave velocity change during loading and unloading from 44 to 191 MPa is approximately linear after Stage I (Fig. 4b).

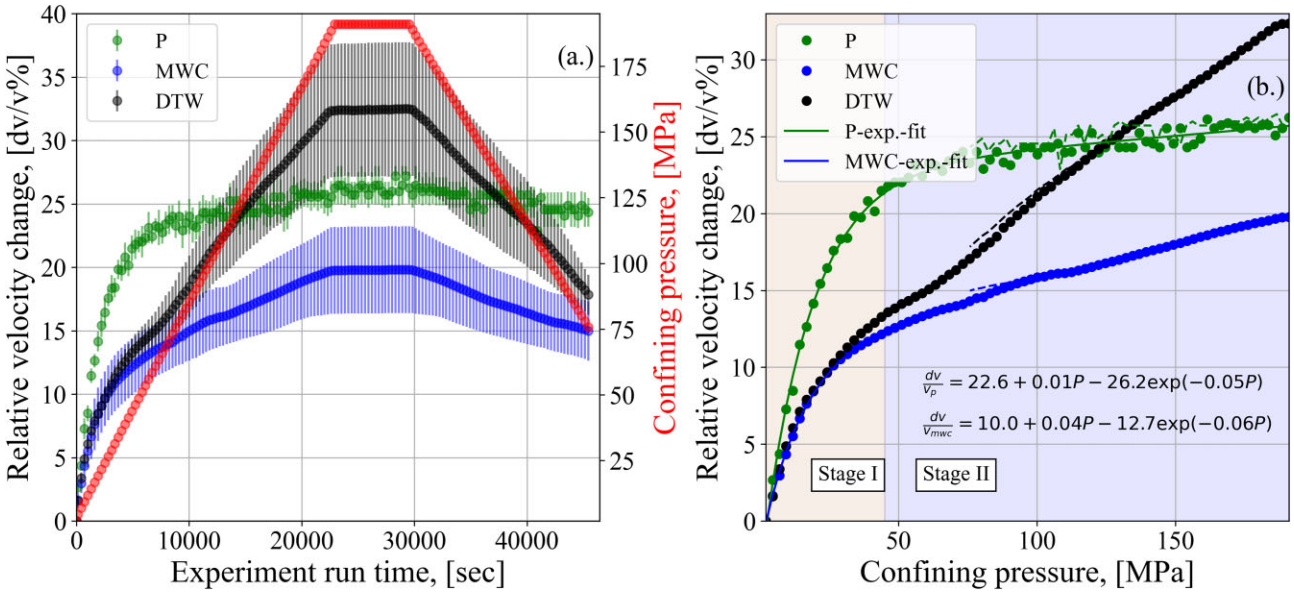

Figure 4. (a) Comparison between the average relative change in velocity (horizontal sensor pairs) and confining pressure increase and decrease (2-191-75 MPa) for experiment Int-2. The vertical lines represent the spread (standard deviation) of velocity between the sender–receiver pair. (b) Average relative change in velocity as a function of confining pressure. The red curve in (a) shows confining pressures during loading and unloading. The black (DTW), blue (MWC) and green (direct *P* wave) curves in (a) and (b) represent the relative percent change in d*v*/*v*, fitted with an exponential function (eq. 7) in (b). The circle represents the cycle with confining pressure increase and the dashed lines represent the depressurization cycle. The initial closure of irregular cracks and pores and the collapse of weak minerals are associated with Stage I. Stage II represents the compression of isometric pores and competent minerals. Distinct stages are distinguished based on Bayesian Information Criteria (BIC; see Suppl. 3).

The two stages of velocity change from 2 to 191 MPa can be described by a combination of a linear and exponential function:

$$V(P_c) = A + K P_c - B \exp(-P_c D) \quad (7)$$

as suggested by Kaselow & Shapiro (2004), where A, B, K and D are fitting parameters and P_c is confining pressure. This equation provides a good estimate of the overall velocity change during distinct stages of crack closure and pore space compression which is further explained in the discussion section.

Changes associated with coda waves differ from those associated with the direct *P* phase. The velocity change represented by the coda waves appears to be directly correlated with confining pressure after the initial crack closure Stage I (i.e. $P_c > 44$ MPa, Fig. 4). The two applied methods for coda waves, MWC and DTW, display a similar shape of velocity change in Stage I, followed by a more rapid, linear velocity increase for DTW during Stage II. Consequently, the peak velocity change for DTW is 32.4 per cent and only 20 per cent for MWC.

The difference between MWC and DTW shows that MWC likely provides an average velocity for the specific window used for cross-correlation, resulting in a smaller velocity change than the DTW method. CWI is more sensitive to the deformation of isometric pore space at high confining pressures when compared to direct phase velocity (Fig. 4b). As shown by the standard deviation in Fig. 4(a), the rate of velocity change (horizontal traces) along different sensor pairs varies, indicating that the velocity change in the medium may not be homogeneous and may have a higher measurement error. Direct *P*-wave velocity has the lowest standard deviation compared to the other two methods, while DTW has the highest. This difference indicates that the direct ray paths for the *P*-wave experience a change in the medium that is nearly identical throughout the medium. Both DTW and MWC sample the velocity change of the coda waves caused by the multiply scattered waves, measured over a larger volume and exhibiting a greater variation in d*v*/*v* with various sensor pairs.

3.2 Effects of confining pressure increase on saw-cut samples

We investigate relative velocity variations due to fault roughness and pressure changes (Table 2) for two polished (FaultS-1 and FaultS-2) and three roughened surfaces (FaultR-1, FaultR-2 and FaultR-3). Velocity changes were again determined from pulses transmitted through the sample at 30-s intervals via an ultrasonic pulse generator. The respective waveform records show ideal characteristics for interferometric analyses in the form of gradual temporal changes and consistently high coherency (cross-correlation coefficient >0.9) within 150 μs of *P*-arrivals (Figs 5a and d).

The time shifts calculated from DTW and MWC are not directly comparable, as the time-shift estimated from DTW is slightly higher than that estimated from MWC. When increasing the confining pressure from 2 to 120 MPa, we observe systematic changes in the lag times of the coda wave computed from DTW and MWC (Fig. 5). At the beginning of confining pressure increase, coda wave lag times increase rapidly in line with the visually apparent compression of the recorded seismograms. The changes in coda wave characteristics are most pronounced between ~35 and 200 μs. Changes in d*t*/*t* with confining pressure are less rapid at elevated pressures above 60 MPa. Both MWC and DTW resolve similar lag-time patterns without obvious differences between rough and polished saw-cut faults (Fig. 5).

We compare relative velocity variations due to fault roughness and pressure changes, finding much stronger effects from confining pressure increase. We computed the relative velocity changes in Fig. 6 by averaging the velocity changes from all horizontal sender–receiver pairs. Average roughness-driven velocity changes

Table 2. Summary of the relative change in velocity for direct *P*, and coda waves (MWC and DTW) calculated for several tests at a confining pressure of 10, 30, 60, 90 and 120 MPa.

P_c [MPa]	10			30			60			90			120		
	P	MWC	DTW	*P*	MWC	DTW	*P*	MWC	DTW	*P*	MWC	DTW	*P*	MWC	DTW
Int-1	7.6	4.7	5.2	18.3	10.6	11	23	13.4	15	23.1	15.2	19.4	25.2	16.5	23.8
FaultS-1	-	1.4	0.7	-	4.5	6.3	-	8	10.5	-	9.9	13.5	-	11.7	15.6
FaultS-2	6.8	1.7	1.1	14.3	4.9	6.9	17.9	8	11	20	10.5	14.2	21.6	12.6	16.6
FaultR-1	-	1.9	3.2	-	5.7	8.3	-	9.3	13.2	-	11.8	16.4	-	13.8	19.1
FaultR-2	6.3	2.1	1.1	16	6.3	7.9	20	10	12.5	21.8	13.1	16.4	23.2	15.2	19.2

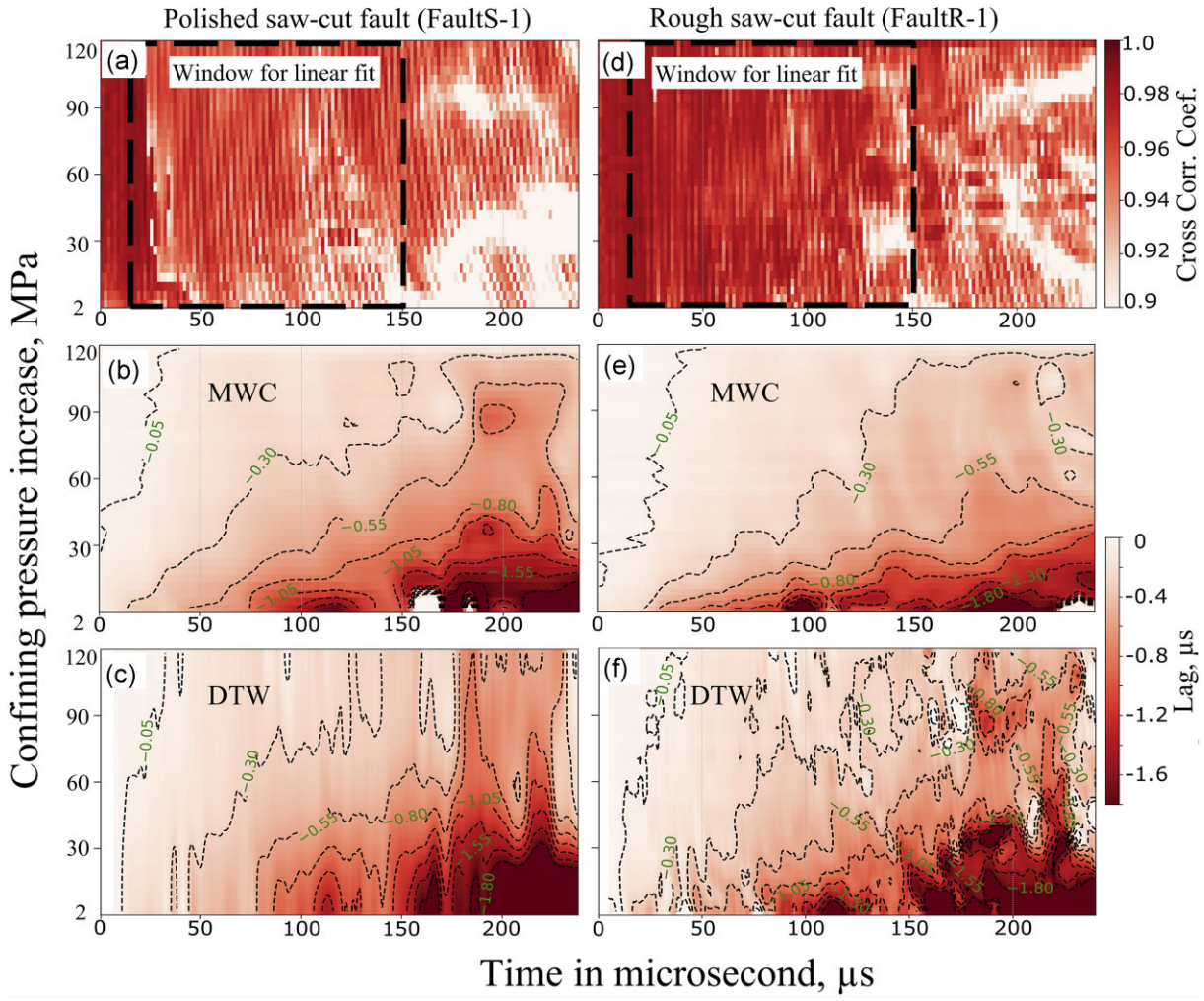

Figure 5. (a, d) Cross-correlation coefficient obtained from moving window cross-correlation method (MWC) for polished (FaultS-1) and rough faults (FaultR-1) for sender-4 and receiver-2 pair (see Suppl. 5). The black box highlights the region used to determine relative velocity changes by linearly fitting lag time vs. run time. (b, c) Time-shift estimated from the windowed cross-correlation method for polished (FaultS-1) and rough faults (FaultR-1). Panels (c) and (e) are the same as (b) and (e) but with lag times from dynamic time warping (DTW). Both methods and experiments demonstrate the sensitivity of coda waves to confining pressure increases, especially during the initial increase from 2 to 60 MPa.

(i.e. differences between smooth and rough faults) are between 1 and 3.6 per cent (Fig. 6; Table 2). However, this difference is less than the velocity variation between different sender–receiver pairs. The weaker influence of fault stiffness on seismic velocity may cause a slight difference in velocity. In contrast to fault roughness, pressure-induced velocity changes can be up to 12 cent (Fig. 6; Table 2). Thus, seismic velocity changes are more susceptible to pressure than variation in the surface roughness of saw-cut faults.

We find that velocity changes determined from DTW are slightly higher and more consistent between various experiments than from MWC. MWC shows a change in velocity of about 14–15 per cent for rough and 12 per cent for smooth faults. On the other hand, when using the DTW method, the change in velocity is up to 19 per cent for rough and 16–17 per cent for polished faults, with rough faults always exhibiting higher velocity changes. Irrespective of the magnitude of velocity change, the overall pattern of the velocity increase is the same for MWC and DTW.

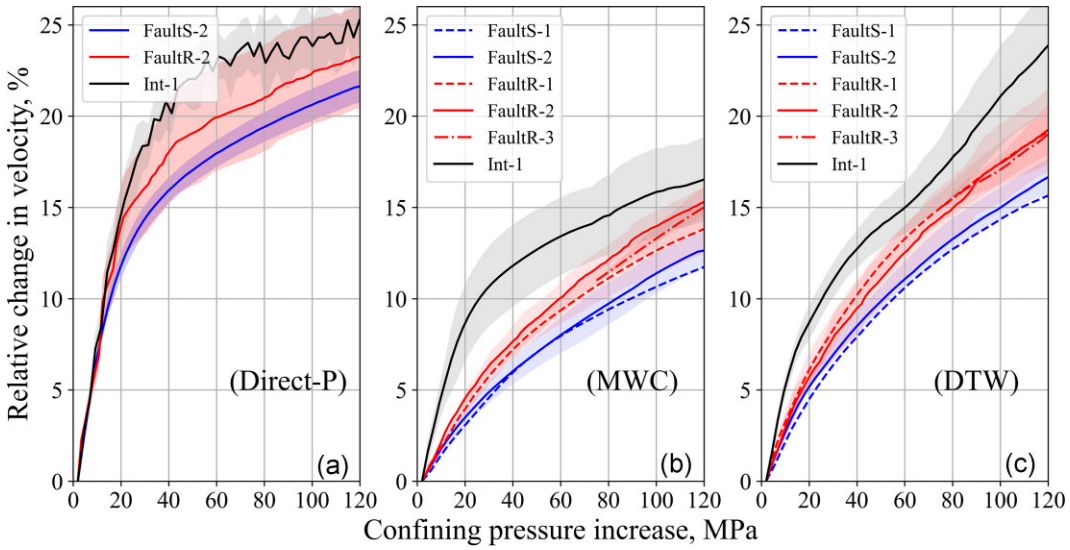

Figure 6. (a) For all horizontal traces, the average *P*-wave velocity change for both rough and smooth faults. The colour shades represent the standard deviation of change in velocity for different senders. (b) Average relative change in velocity obtained for different saw-cut faulted samples, rough and smooth, at different states of confining pressure obtained from a short time windowed cross-correlation method. The black dashed line with a grey shade shows the average d*v*/*v* and standard deviation for intact rock computed from CWI. (c) Average relative change in velocity obtained for different faulted samples, rough and smooth, at different states of confining pressure obtained from the DTW method.

3.3 Increasing axial load leading to failure of an intact rock

We examine progressive damage accumulation and velocity changes with increasing stress before intact rock fracture. A granite core (Frac-1) was initially compressed hydrostatically from 2 to 75 MPa and then axially loaded to failure at 780 MPa differential stress while recording both AE events and active ultrasonic transmissions.

In the following, we describe several distinct measurements: We first determine direct *P*-wave velocity in the vertical (i.e. parallel to the load axis) and horizontal directions to investigate seismic anisotropy before failure. We then compare MWC and DTW to determine how the velocity of coda waves varies with increasing differential stress. Finally, we compare acoustic emission, differential stress and seismic velocity leading up to failure.

Vertical and horizontal *P*-wave velocities are highly anisotropic at high differential stress (Fig. 7). Although vertical velocity increased by 1.2 per cent within 280 MPa before decreasing by −4.8 per cent (Fig. 7a), horizontal velocities monotonously decreased to −27 per cent over the same period. This strong anisotropy results from the accumulation of microcrack damage with preferred orientations subparallel to σ_1 (Fig. 7).

Similar to vertical *P*-wave velocities, coda waves exhibit a decrease of up to 5 per cent with increasing differential stress in the horizontal direction (Fig. 8). We used the Bayesian Information Criteria (BIC) to distinguish different phases of velocity change (see Suppl. 7e). Phase I characterizes a modest velocity increase (maximum positive velocity change) likely driven by dominant axial pore space compaction prior to 235 MPa. Phase II marks the onset of velocity decrease between 235 and 535 MPa, followed by Phase III, during which velocity decreases more rapidly with higher differential stress. Notably, the beginning of Phase III matches the onset of AE activity (which accelerates toward failure), and deviation from linear stress increase with applied load. The later portion of Phase III marks fracture nucleation leading to the failure of the sample (Supplementary Video). MWC and DTW results in similar estimates of the changes in velocity (Fig. 7).

Load-cell and velocity measurements throughout the experiment demonstrate notable changes in the bulk properties long before macrofailure (Brace *et al.* 1966; Paterson & Wong 2005; Aben *et al.* 2020). Axial stress determined from an external load cell deviates from linearity at around 502 MPa (yield stress from BIC: see Suppl. 7a and c). This is 290 MPa after the initial drop detected in seismic velocities (i.e. the onset of Phase II), about one-third to two-thirds of differential stress at failure (Brace *et al.* 1966; Paterson & Wong 2005). Both measurements indicate a long-lasting process of slow damage accumulation with increasing differential stress. However, seismic velocities are much more sensitive to this process than macroscopic measurements.

In addition to changes in seismic velocity, we observe a pronounced spatial evolution of acoustic emission locations from random spatial occurrences to spatially-clustered behaviour (see Fig. 8 and Supplementary Video). Here, the onset of AEs generally corresponds to a mechanical yield stress, while velocity decreases begin at lower stress levels (Fig. 8). This suggests that microcrack damage before the onset of AEs is aseismic, or undetectable by the AE monitoring system. The Supplementary Video shows that AEs start to cluster after 7000 s (675 MPa). The first cluster of AEs can be observed at 43 mm from the top of the sample. From 7800 (740 MPa) to 8200 s (765 MPa), two new clusters form, one along the upper edge of the sample (80–105 mm) and the other along the lower half (0–40 mm). The video shows that the top cluster contains a substantial number of AEs (Fig. 8) within two linear structures (Supplementary Video). At 778 MPa, these two linear clusters combine to form the nucleus of the macroscopic fracture. The acoustic emission rates reveal that most AEs were detected in the upper (80–105 mm) portion of the sample, while the least number of AEs before failure was detected in the middle portion of the sample (40–60 mm; Fig. 8).

Both acoustic emission activity and seismic velocities show a high sensitivity to accumulating microcrack damage before failure (Fig. 8). To minimize end-surface effects, we placed Teflon sheets between the sample and the loading pistons and generally found no AE clustering close to the lower or upper end of the sample. A

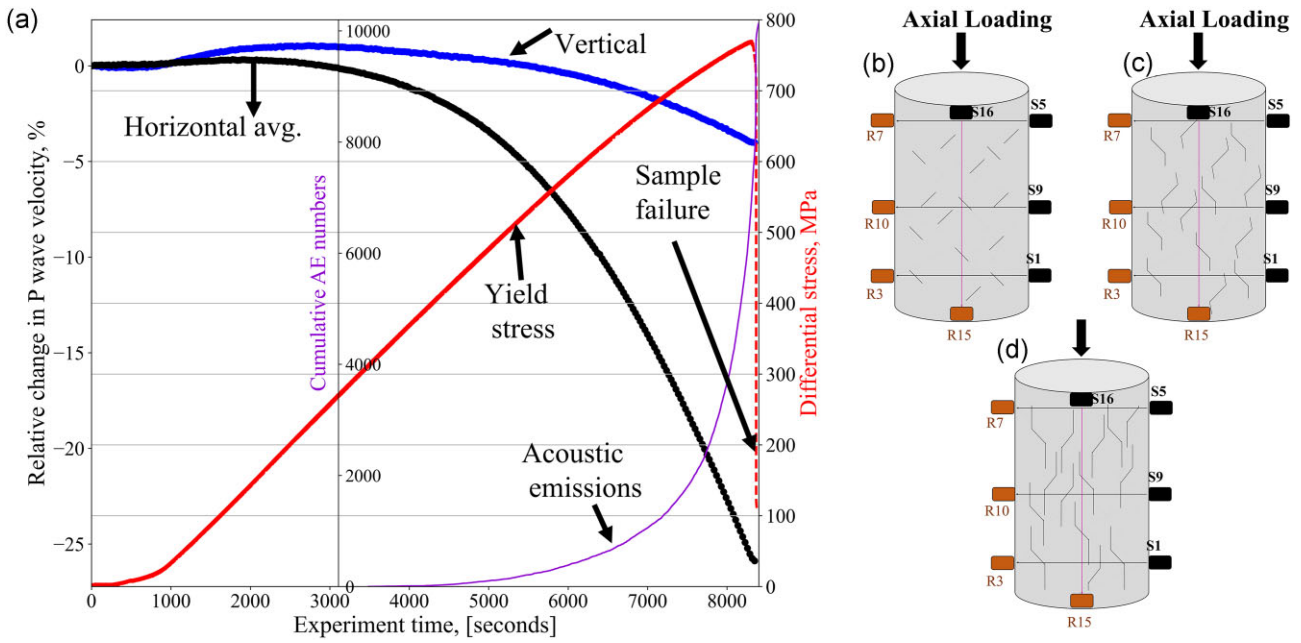

Figure 7. (a) Relative change in *P*-wave velocity in the horizontal (black) and vertical (blue) directions for intact rock fracture experiment (Frac-1). Increasing differential stress (red) drives damage accumulation and higher crack density. These cracks are preferably aligned with the direction of axial load leading to pronounced seismic anisotropy in the sample before failure after 8325 s (780 MPa). The acoustic emission (purple) starts to emit rapidly after the load exceeded the yield stress (502 MPa: see Suppl. 7). (b)–(d) Schematic of progressive crack growth and coalesce leading to velocity decrease and anisotropy before failure (Ashby & Sammis 1990) with increasing axial load.

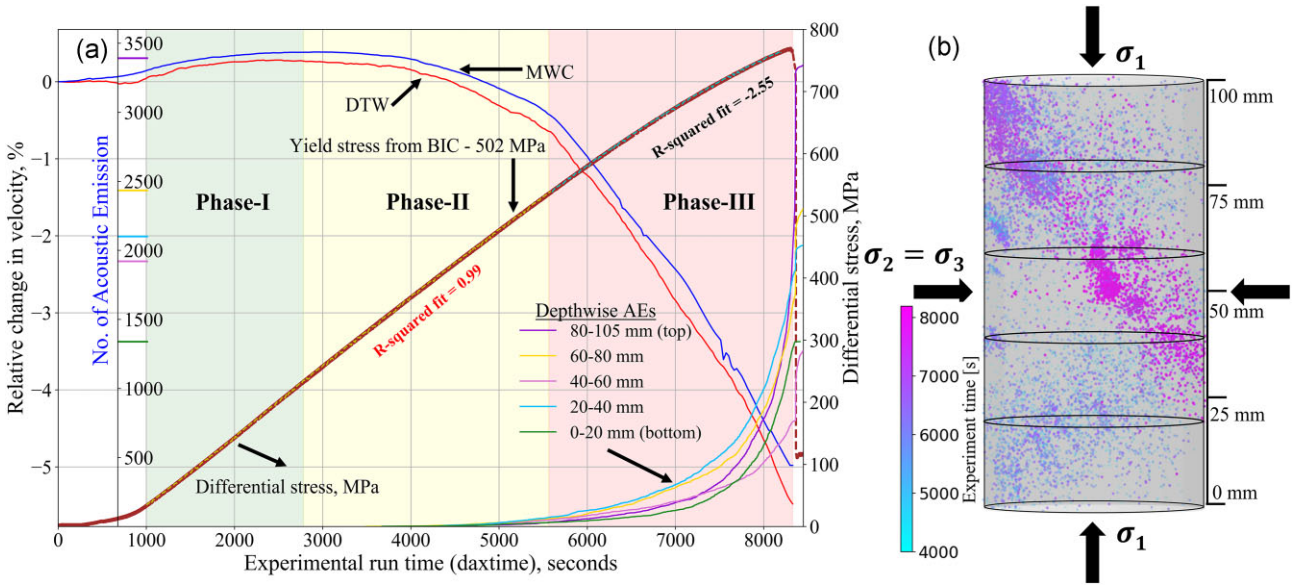

Figure 8. Microcrack compaction and creation can be separated into 3 phases based on average relative velocity changes in the horizontal direction (blue=MWC and red=DTW) and differential stress (black curve) for intact rock fracture experiment (Frac-1). Phase I is associated with initial crack closure, increasing velocity, and linear stress increase. Phase II marks the start of velocity decrease while stress increase remains linear. Phase III marks the onset of AE activity (coloured by depth) which accelerates toward failure, deviation from linear stress increase, and a more rapid drop in seismic velocity. Inset: Acoustic emission locations during early nucleation [blue: 6000s (582 MPa)–8000s (753MPa)], and fracture propagation (purple: 8000+ s). The horizontal lines between 3000 (260 MPa) and 4000 (371 MPa) *s* display the maximum number of AEs for each depth distinguished by colours.

higher decrease in velocity, up to −25 per cent, is associated with a higher rate of AE events at the top (sender:5, receiver:7) and bottom (sender:1, receiver:3) sections of the sample (Figs 9a and e). On the other hand, the middle part of the sample (sender:9, receiver:10) has the least drop in velocity (Fig. 9c), up to −20 per cent, where the number of acoustic emissions is the lowest.

We observe pronounced seismic anisotropy for the direct *P* wave for which the horizontal ray paths (S5R7, S9R10 and S1R3) show a significant velocity decrease with increasing stresses (−27, −20 and −25 per cent, respectively; Fig. 9). Ray paths that are at small angles to the σ_1 direction (S5R15, S1R7) show a more modest decrease (−8 per cent). Careful analysis of *P*-wave velocity change as a

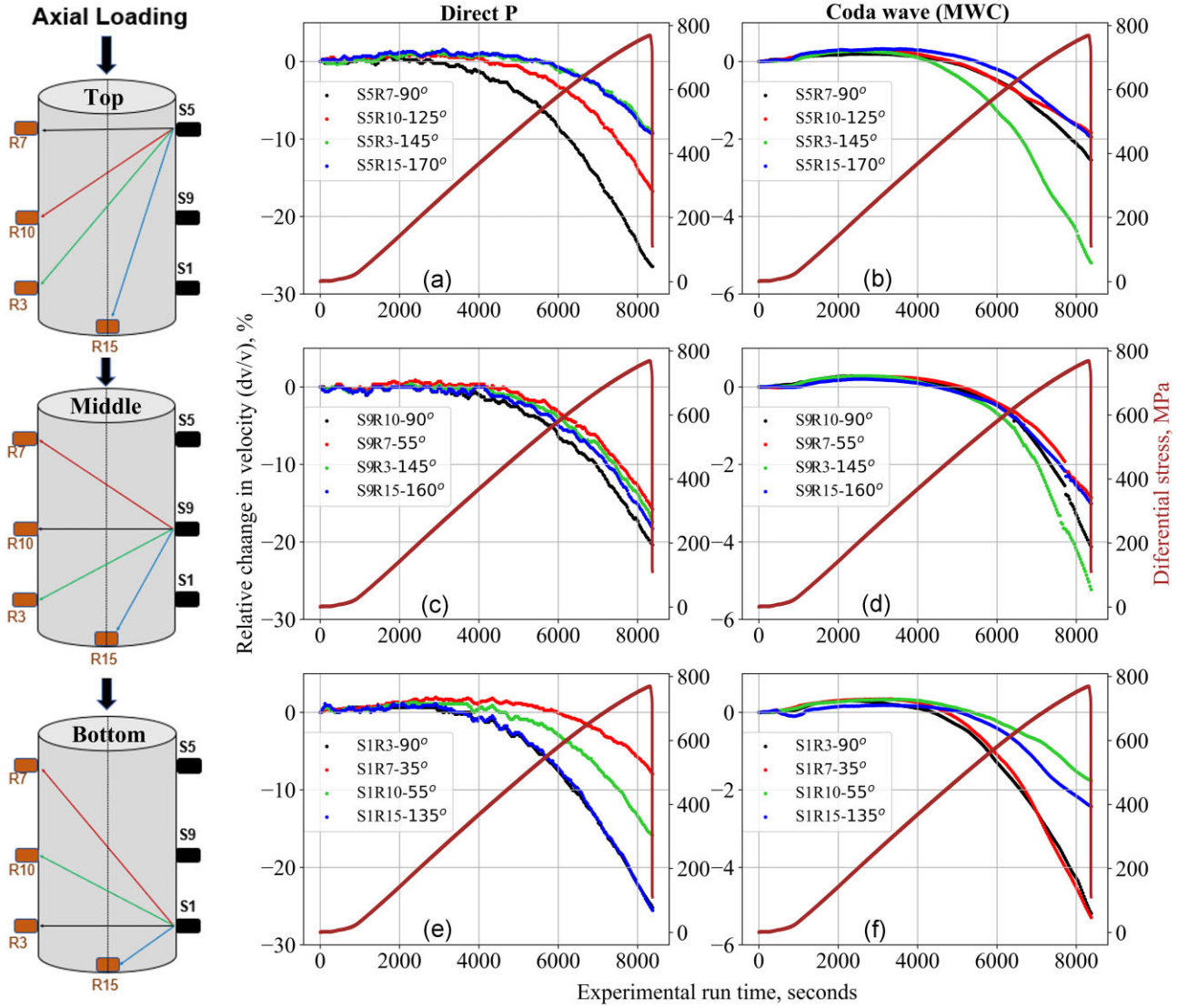

Figure 9. Measurement of the relative change in velocity at different sections (top, middle and bottom) and along different ray paths (i.e. sensor–receiver orientations represented by red, green, black and blue colour) for intact rock fracture experiment (Frac-1). a, c and e) Relative velocity change computed for direct *P* phase for different sender–receiver pairs. b, d and f) Change in velocity for coda wave computed from MWC method. Different colours correspond to different combinations of sender–receiver pairs or different ray paths. The brown curve represents the differential stress acting upon the sample. On the right, three cylinders show where the sender and receiver are at different sample parts.

function of angle to σ_1 shows that the fastest direction is along the vertical and gets slower as the ray path gets horizontal. In contrast, coda wave velocity estimates show no systematic variations for different sender–receiver pairs. The overall coda velocity decrease of up to −5.5 per cent is smaller than horizontal *P*-wave reductions but roughly agrees with vertical *P*-wave velocity changes (Fig. 7a). The results suggest that coda and direct wave velocity estimates exhibit different sensitivities to the type and orientations of damage and microcracks during axial and hydrostatic loading.

4 DISCUSSION

We studied damage evolution in three different experiments using two ways to measure the relative change in velocity. The result allows us to determine the relationship between pore volume and seismic velocity, the dependency of seismic velocity on normal stress, and the properties of coda waves at various stages of damage evolution.

4.1 Dependence of velocity change on pore volume geometry and elastic moduli in intact rock compression

The observation of velocity change in an intact rock under hydrostatic pressure shows both non-linear and linear behaviours under low and high confining pressure, respectively (Fig. 4b; Birch 1960, 1961; Brace *et al.* 1968; Paterson & Wong 2005). We hypothesize that this change in velocity is proportional to the porosity, and bulk moduli of the sample when increasing the confining pressure (Kaselow & Shapiro 2004; Stanchits *et al.* 2006; Walsh 1965; Watanabe & Higuchi 2015). Grain boundary cracks with small apertures and high aspect ratios are rapidly closing even at low confining pressure, resulting in a significant increase in velocity at Stage I (Fig. 10). At P_c higher than 44 MPa (Stage II), the relative

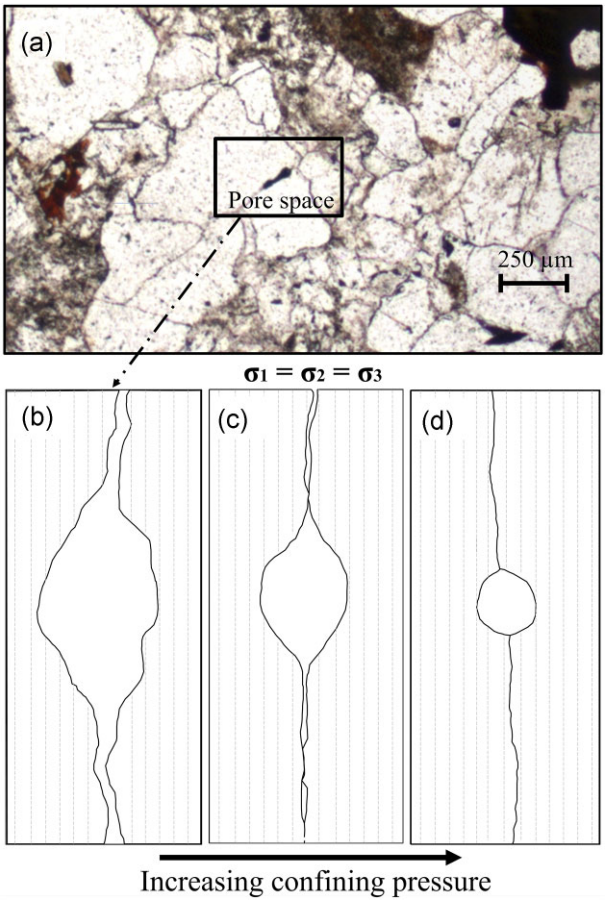

Figure 10. (a) Optical microscopy of an intact Westerly granite sample observed under plane-polarized light. A black box depicts a representative pore geometry for discussing the condition as confining pressure increases. (b) Schematic pore geometry with no applied confining pressure. (c) Schematic pore geometry with increasing confining pressure showing linear pore space collapse. (d) The compliant pore volume closes completely at high confining pressure.

velocity change shows a linear behaviour for several rock types (Birch 1960; Walsh 1965; Kaselow & Shapiro 2004; Watanabe & Higuchi 2015; Hefny *et al.* 2020). When P_c is reduced, the velocity decrease follows the same path as during pressure increase, indicating elastic behaviour (i.e. no hysteresis) of rock at higher P_c (Fig. 4b). At higher P_c (Stage II), the linear portion represents the intrinsic seismic characteristics (Birch 1960, 1961), meaning that the change is associated with the compression of competent gains and isometric pore space (stiff porosity, Fig. 10d).

The quantitative model by Kaselow & Shapiro (2004) describes the two-deformation phases by combining linear and exponential terms (see eq. 7). The ratio of compliant porosity and elastic moduli in the model (i.e. the D parameter; Greenfield & Graham 1996; Kaselow & Shapiro 2004) is roughly the same for all elastic moduli and velocities (Eberhart-Phillips *et al.* 1989; Greenfield & Graham 1996; Kaselow & Shapiro 2004; Sun *et al.* 2012), even when the velocity is estimated from different methods. The velocity change under hydrostatic compression follows the four parametric exponential functions (see eq. 7). The exponential term (D) for the Int-1 and Int-2 experiments are constant at 0.06 ± 0.01 according to our velocity versus confining pressure fit (Fig. 4b and Suppl. 3). The linear term and parameters A, K and B vary for coda wave velocity (MWC), and P-wave velocity shows no similarity and varies over the experiment (Suppl. 4).

4.2 Dependence of velocity change on confining pressure and rough saw-cut faults

The change in velocity across saw-cuts at low P_c is dominated by the failure of asperities, leading to an increase in the real area of contact and the formation of gouge. In microscopic images of regions with rough surfaces under normal stress, the real area of contact grows linearly due to the growth, coalescence and creation of larger contacts (Dieterich & Kilgore 1994, 1996). Likewise, these authors showed that there are effects of confining pressure increase on contact surface properties on the faults. Here, the change in velocity at low P_c shows that the seismic velocity depends on how quickly the contact area evolves with increasing confining pressure. As the confining pressure increases, asperity evolution becomes less important for velocity changes, and the effects of the matrix-pore space reduction dominate (Fig. 10). At higher confining pressure, such asperities evolve plastically with reducing geometrical aperture (Kang *et al.* 2016; Acosta *et al.* 2020) and increased effect of bulk pore spaces on seismic velocity change.

4.3 Damage-dependent anisotropy in intact rock fracture

P wave and coda wave velocity changes are correlated with different stages of micromechanical damage formation before intact rock fracture (Fig. 8). For brittle deformation of intact rock samples, the mechanical yield point is often considered the onset of microcrack formation given by Ashby & Sammis (1990):

$$\sigma_1 = \left(\frac{\left(1+\mu^2\right)^{\frac{1}{2}} + \mu}{\left(1+\mu^2\right)^{\frac{1}{2}} - \mu} \sigma_3 \right) - \frac{\sqrt{3}}{\left(1+\mu^2\right)^{\frac{1}{2}} - \mu} \frac{K_{IC}}{\sqrt{\pi a}}, \tag{8}$$

where σ_3 is the confining pressure, K_{IC} is the fracture toughness of the material through which the crack propagates, a is the half length of the original inclined crack and μ is the coefficient of friction acting between the crack faces. Consequently, we expect crack growth to commence at $\sigma_1 = 230$–343 MPa using $\sigma_3 = 75$ MPa, $K_{IC} = 1.8$ MPa $m^{\frac{1}{2}}$, Byerlee's range of coefficient of friction ($0.6 \leq \mu \leq 0.85$), and an initial flaw size of 0.3 mm for our experiment. This value is substantially lower than the macroscopically observed value of ~500 MPa, but coincides with the onset of gradual velocity reduction (Phase II: Fig. 7a).

In agreement with previous studies (Stanchits *et al.* 2006), we find that the onset of an accelerated AE activity corresponds roughly with the yield point (502 MPa) but the velocity decrease occurs much earlier at comparably low differential stresses. This may indicate that some aseismic opening of microcracks may start below the yield stress (Brace *et al.* 1966; Paterson & Wong 2005; Aben *et al.* 2020). With progressive loading beyond the yield stress (Fig. 8, Phase III) the microcracks will eventually coalesce within a localized zone, marking the onset of macroscopic failure (Lockner *et al.* 1991; Aben *et al.* 2020). Postmortem microstructure analysis of fractured samples shows that crack density may increase up to ten times (Dresen & Gueguen 2004). Furthermore, the analysis of horizontally propagating P waves reveals that the velocities decrease by nearly a factor of ten between yield stress (−2.5 per cent at around 480 MPa) and failure (−25 per cent at failure, Fig. 7a). We observe a pronounced seismic anisotropy due to preferential crack shapes and orientations (Fig. 7). The seismic anisotropy increases

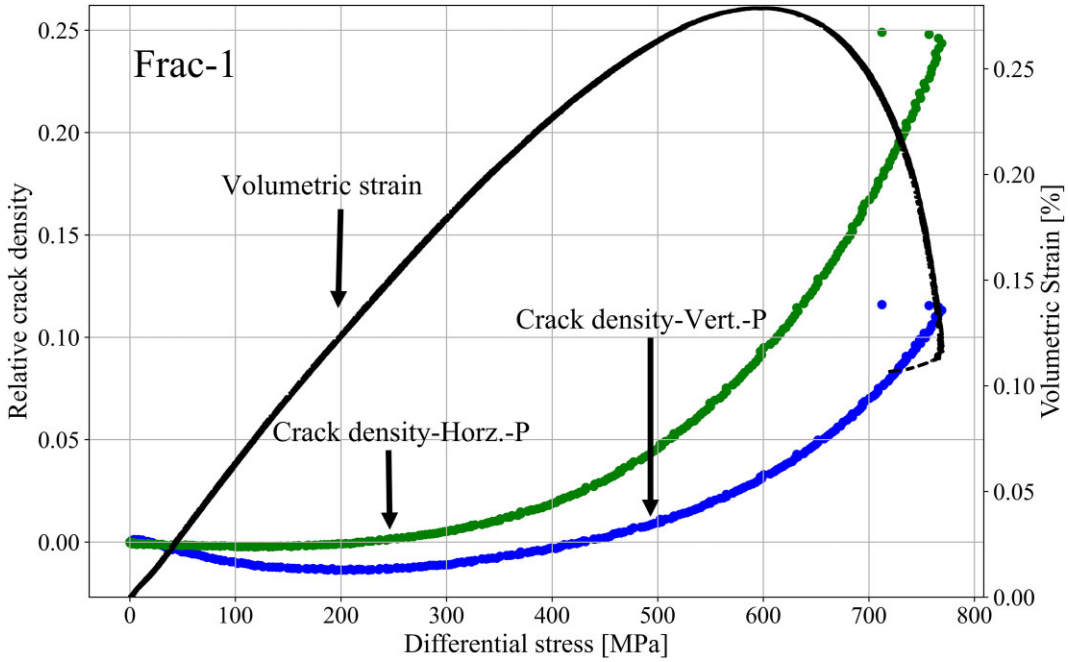

Figure 11. Comparison between the observed damage accumulation recorded by the strain gauges and crack density computed from the direct *P*-wave velocity. The plot of volumetric strain (black curve and right *y*-axis), and crack density from *P*-wave velocity (blue and green curves and left *y*-axis) plotted against differential stress for the intact rock fracture experiment (Frac-1). Volumetric strain ($= {}_1 + 2{}_2$) was calculated by using the axial strain ($_1$) and radial strain ($_2$) measured during the experiment.

after 335 MPa up to failure (Phase II, III). As the experiment moves to Phase III, abundant wing cracks form with a preferred orientation subparallel to σ_1, leading to a higher level of anisotropy in the medium. Seismic interferometric measurements are thought to be highly sensitive to changes in the medium (Grêt 2003; Grêt *et al.* 2006), but we found that such measurements are also dependent on the type of fracture geometry (i.e. orientation and shape; Soga *et al.* 1978; Stanchits *et al.* 2006) and scatterer (i.e. opening and collapse of pores and fractures; Singh *et al.* 2019; Zotz-Wilson *et al.* 2019).

The study of simple rock compression experiments, such as the compression of intact rocks and rocks with saw-cut faults, shows that velocity changes from CWI are better correlated with changes in bulk pressure than direct *P*-wave velocity. Our observations could be explained by the deformation of isotropic pore volume, and minerals throughout the sample in rock compression experiments. We observe increasingly anisotropic behaviour of direct seismic velocity measurements for a sample that is loaded to failure. Notably, velocity estimates from CWI are not anisotropic but rather produce velocity variations that are consistently more similar to the vertical direct *P*-wave velocity.

Our observations indicate that coda and direct waves exhibit different sensitivities to fracture and pore space geometry, especially to cracks with preferred orientations (Singh *et al.* 2019; Zotz-Wilson *et al.* 2019). Moreover, direct and coda waves follow distinct ray paths which may substantially affect the respective results.

4.4 Microcrack assessment from *P*-wave velocity and volumetric strain measurement in intact rock fracture

Previous studies showed that crack density estimates based on seismic velocities measurements in two orthogonal directions could track anisotropy due to increasing stress and axial strain (Soga *et al.* 1978; Stanchits *et al.* 2006). We used the model from Soga *et al.* (1978) to invert for the crack density parameter (Γ) from the velocity data:

$$\Gamma_H = \frac{(a_1 - a_2) + a_2\left(\frac{P_V}{P_0}\right)^2 - a_1\left(\frac{P_H}{P_0}\right)^2}{a_1^2 + a_1 a_2 - 2a_2^2},$$
$$\Gamma_V = \frac{(a_1 - a_2) - (a_1 + a_2)\left(\frac{P_V}{P_0}\right)^2 + 2a_2\left(\frac{P_H}{P_0}\right)^2}{a_1^2 + a_1 a_2 - 2a_2^2}, \quad (9)$$

where Γ_H and Γ_V are the horizontal (normal to σ_1) and vertical (parallel to σ_1), respectively. P_0, P_V and P_H are the seismic velocities of the crack-free Westerly granite, vertical and horizontal *P*-wave velocity, respectively. The constants a_1 and a_2 are chosen from Soga *et al*. (1978) as 1.452 and 0.192, respectively. For P_0 we assume that the crack-free sample has 5 per cent (Stanchits *et al.* 2006) more velocity than the maximum *P*-wave velocity.

Seismic velocity measurements show much higher sensitivity to damage evolution compared to the strain gauge measurement during axial loading (Zotz-Wilson *et al.* 2019; Fig. 11). Crack densities inferred from velocity measurements indicate a short period of pore space reduction followed by a rapid increase in crack density towards failure (Fig. 11). In contrast, the volumetric strain indicates macroscopic changes until much later (Brace *et al.* 1966; Paterson & Wong 2005; Zotz-Wilson *et al.* 2019) into the loading cycle (i.e. until ∼500 MPa) when velocity-inferred crack density already indicates significant new microcrack generation. This early crack growth is thus largely undetectable macroscopically and also occurs much before the onset of AE activity.

4.5 Comparison between direct *P*-wave and coda wave measurements

Previous results revealed several fundamental differences in velocity estimates between direct phase and coda wave estimates. Coda waves are sensitive to average relative velocity changes across the medium due to the scattering of the waves, thereby sampling a broad volume. Coda waves are assumed to be less sensitive to localized anomalies and represent broader areas due to multiply scattered waves (Snieder *et al.* 2002; Grêt 2003; Grêt *et al.* 2006). Strong heterogeneity in the medium creates a challenge for the spatial averaging of propagating coda waves, which may not uniformly sample velocity changes across the entire rock if damage or microcracks are large. Direct *P* waves, on the other hand, are sensitive to average velocity changes along a localized ray path either due to large but localized velocity changes or due to broader small-amplitude velocity perturbations.

Our results suggest two additional differences between direct phase and coda wave techniques. First, direct *P*-wave velocity is highly sensitive to stress-induced anisotropy, whereas coda waves show no anisotropic effects and are generally comparable to the vertical (i.e. the fast direction) *P*-wave velocity. Secondly, relative velocity changes are more pronounced for the direct *P* phase than the coda waves. Smaller relative velocity changes in Coda wave estimates may be due to different spatial and temporal averaging of the actual measurement and different propagation effects.

Combining direct *P* wave and coda wave measurements could provide new insights and understanding of subsurface structure. The property of the *P* wave in sampling anisotropy and coda wave sensitivity to scatterers provides information about wave interaction with broader perturbations. Both wave types will contribute unique information, and their integration may provide a more comprehensive understanding of subsurface features.

5 CONCLUSION

In this study, we investigated the evolution of microcracks with increasing stress and pressure in different Westerly granite samples using direct *P*-wave and coda wave velocity estimates.

The results obtained from the compression experiments on saw-cut samples suggest that changes in the bulk material of the rock sample have a more significant impact on seismic velocity than changes in fault roughness. As confining pressure increases, the failure of asperities and the subsequent fault closure have minimal effects on the velocity change. The asperities undergo plastic deformation, resulting in a decrease in their geometric apertures (Kang *et al.* 2016; Acosta *et al.* 2020).

Seismic velocities can be used to detect changes in microcrack damage prior to the onset of measurable changes in volumetric strain. The seismic velocity change demonstrates the progressive growth of microcracks on an intact rock fracture experiment with three major phases. In contrast, strain gauge measurements could only detect dominant crack openings at the later stage of the experiment, suggesting small changes were not detectable by volumetric strain.

Moreover, our results show that the direct *P*-wave velocity exhibits strong anisotropy with increasing differential stress. The careful analysis of vertical and horizontal *P*-wave velocity allows us to understand the formation and coalescence of wing cracks. In contrast, coda wave velocity does not show seismic anisotropy and roughly agrees with vertical *P*-wave velocity change. This suggests that coda and direct wave velocities are sensitive to different types and orientations of damage and microcracks during axial and hydrostatic loading.

Our findings could help advance understanding of the usefulness of coda wave velocity and direct *P*-wave velocity in assessing damage accumulation under varying stress and pressure conditions. Likewise, using dense geometric distribution of sensors with different source and receiver pairs for CWI would benefit the study of fractures and fault damage.

ACKNOWLEDGMENTS

We would like to convey our appreciation for the assistance from numerous organizations throughout this project. We especially thank the United States Geological Survey (G21AP10050 and G21AP10032) for their financial support. We also acknowledge the German Research Centre for Geosciences for providing us with the opportunity and facilities for the research. THG acknowledges support from an NSF Early Career Award (Award Number: 2142489).

DATA AVAILABILITY

The data and code used in this study are accessible from the authors upon request. For access, please contact the authors.

SUPPORTING INFORMATION

Supplementary data are available at *GJI* online.

suppl_data

Please note: Oxford University Press is not responsible for the content or functionality of any supporting materials supplied by the authors. Any queries (other than missing material) should be directed to the corresponding author for the paper.

REFERENCES

Aben, F.M., Brantut, N. & Mitchell, T.M., 2020. Off-fault damage characterization during and after experimental quasi-static and dynamic rupture in crustal rock from laboratory P wave tomography and microstructures, *J. geophys. Res.,* **125**(8), doi:10.1029/2020JB019860.

Acosta, M., Passelègue, F.X., Schubnel, A., Madariaga, R. & Violay, M., 2019. Can precursory moment release scale with earthquake magnitude? A view from the laboratory, *Geophys. Res. Lett.,* **46**(22), 12 927–12 937.

Acosta, M., Maye, R. & Violay, M., 2020. Hydraulic transport through calcite bearing faults with customized roughness: effects of normal and shear loading, *J. geophys. Res.,* **125**(8), doi:10.1029/2020JB019767.

Adourian, S., Lyu, C., Masson, Y., Munch, F. & Romanowicz, B., 2022. Combining different 3D global and regional seismic wave propagation solvers towards box tomography in the deep Earth, *J. geophys. Int.,* **232**(2), 11 340–11 356.

Akaike, H., 1974. A new look at the statistical model identification, *IEEE Trans. Autom. Contl.,* **19**(6), 716–723.

Aki, K. & Lee, W.H. K., 1976. Determination of three-dimensional velocity anomalies under a seismic array using first P arrival times from local earthquakes: 1. A homogeneous initial model, *J. geophys. Res.,* **81**(23), 161–177.

Ashby, M.F. & Hallam, S.D., 1986. The failure of brittle porous solids under compressive stress states, *Acta Metallur.,* **34**(3), 511–526.

Ashby, M. & Sammis, C., 1990. The damage mechanics of brittle solids in compression, *Pure appl. Geophys.,* **133,** 489–521.

Barklage, M., Wiens, D.A., Conder, J.A., Pozgay, S., Shiobara, H. & Sugioka, H., 2015. P and S velocity tomography of the Mariana subduction system from a combined land-sea seismic deployment, *Geochem. Geophys. Geosyst.,* **16,** 681–704.

Ben-Zion, Y. & Sammis, C.G., 2003. Characterization of fault zones, *Pure appl. Geophys.,* **160,** 677–715.

Bhat, H.S., Sammis, C.G. & Rosakis, A.J., 2011. The micromechanics of Westerley granite at large compressive loads, *Pure appl. Geophys.,* **168,** 2181–2198.

Birch, F., 1960. The velocity of compressional waves in rocks to 10 kilobars: 1, *J. geophys. Res.,* **65**(4), 1083–1102.

Birch, F., 1961. The velocity of compressional waves in rocks to 10 kilobars: 2, *J. geophys. Res.,* **66**(7), 2199–2224.

Bolton, D.C., Shreedharan, S., Rivière, J. & Marone, C., 2020. Acoustic energy release during the laboratory seismic cycle: insights on laboratory earthquake precursors and prediction, *J. geophys. Res.,* **125**(8), doi:10.1029/2019JB018975.

Brace, W.F., Paulding, B.W. Jr & Scholz, C.H., 1966. Dilatancy in the fracture of crystalline rocks, *J. geophys. Res.,* **71**(16), 3939–3953.

Brace, W.F., Walsh, J.B. & Frangos, W.T., 1968. Permeability of granite under high pressure, *J. geophys. Res.,* **73**(6), 2225–2236.

Brantut, N., 2018. Time-resolved tomography using acoustic emissions in the laboratory, and application to sandstone compaction, *J. geophys. Int.,* **213**(3), 2177–2192.

Brenguier, F., Campillo, M., Hadziioannou, C., Shapiro, N.M., Nadeau, R.M. & Larose, E., 2008. Postseismic relaxation along the San Andreas Fault at Parkfield from continuous seismological observations, *Science,* **321,** 1478–1481.

Brenguier, F., Shapiro, N.M., Campillo, M., Val, V., Ferrazzini, V., Duputel, Z., Coutant, O. & Nercessian, A., 2008. Towards forecasting volcanic eruptions using seismic noise, *Nat. Geosci.,* **1,** 126–130.

Chayes, F., 1950. Composition of the granites of Westerly and Bradford, Rhode Island, *Am. J. Sci.,* **248,** 378–407.

Diehl, T., Deichmann, N., Kissling, E. & Husen, S., 1950. Automatic S-wave picker for local earthquake tomography, *Bull. seism. Soc. Am.,* **99,** 1906–1920.

Dieterich, J.H., 1972. Time-dependent friction in rocks, *J. geophys. Res.,* **77**(20), 3690–3697.

Dieterich, J.H., 1978. Preseismic fault slip and earthquake prediction, *J. geophys. Res.,* **83**(B8), 3940–3948.

Dieterich, J.H. & Kilgore, B.D., 1994. Direct observation of frictional contacts: new insights for state-dependent properties, *Pure appl. Geophys.,* **143**(3), 283–302.

Dieterich, J.H. & Kilgore, B.D., 1996. Imaging surface contacts: power law contact distributions and contact stresses in quartz, calcite, glass and acrylic plastic, *Tectonophysics,* **256,** 219–239.

Dresen, G. & Gueguen, Y., 2004. Mechanics of fluid-saturated rocks, in *Mechanics of Fluid-Saturated Rocks,* pp. 169–217, eds Gueguen, Y. & Bouteca, M., International Geophysical Series, Elsevier Science.

Dresen, G., Kwiatek, G., Goebel, T. & Ben-Zion, Y., 2020. Seismic and aseismic preparatory processes before large stick-slip failure, *Pure appl. Geophys.,* **177**(12), 5741–5760.

Eberhart-Phillips, D., Han, D.-H. & Zoback, M.D., 1989. Porosity, and clay content in sandstone, *Geophysics,* **54**(1), 82–89.

Ellsworth, W.L., 2019. From foreshocks to mainshocks: mechanisms and implications for earthquake nucleation and rupture propagation, in *Mechanics of Earthquake Faulting, Proceedings of the International School of Physics "Enrico Fermi" Series,* pp. 95–112, IOS Press.

Feng, K.F., Huang, H.H. & Wu, Y.M., 2020. Detecting pre-eruptive magmatic processes of the 2018 eruption at Kilauea, Hawaii volcano with ambient noise interferometry, *Earth, Planets Space,* **72**(74), doi:10.1186/s40623-020-01199-x.

Garnier, V., Piwakowski, B., Abraham, O., Villain, G., Payan, C. & Chaix, J.F., 2013. Acoustic techniques for concrete evaluation: improvements, comparisons and consistency, in *Construction and Building Materials,* Vol. **43,** pp. 598–613, Elsevier.

Goebel, T.H. W., Becker, T.W., Schorlemmer, D., Stanchits, S., Sammis, C., Rybacki, E. & Dresen, G., 2012. Identifying fault heterogeneity through mapping spatial anomalies in acoustic emission statistics, *J. geophys. Res.,* **117**(B3), doi:10.1029/2011JB008763.

Goebel, T.H. W., Sammis, C.G., Becker, T.W., Dresen, G. & Schorlemmer, D., 2015. A comparison of seismicity characteristics and fault structure between stick-slip experiments and nature, *Pure appl. Geophys.,* **172**(8), 2247–2264.

Goebel, T.H. W., Schorlemmer, D., Becker, T.W., Dresen, G. & Sammis, C.G., 2013. Acoustic emissions document stress changes over many seismic cycles in stick-slip experiments, *Geophys. Res. Lett.,* **40,** 2049–2054.

Greenfield, R.J. & Graham, E.K., 1996. Application of a simple relation for describing wave velocity as a function of pressure in rocks containing microcracks, *J. geophys. Res.,* **101**(B3), 5643–5652.

Grêt, A., 2003. Time-lapse monitoring with coda wave interferometry, *Doctoral dissertation,* Colorado School of Mines, Golden, CO.

Grêt, A., Snieder, R. & Scales, J., 2006. Time-lapse monitoring of rock properties with coda wave interferometry, *J. geophys. Res.,* **111**(B3), doi:10.1029/2004JB003354.

Guérin-Marthe, S., Nielsen, S., Bird, R., Giani, S. & Di Toro, G., 2019. Earthquake nucleation size: evidence of loading rate dependence in laboratory faults, *J. geophys. Res.,* **124**(1), 689–708.

Hale, D., 2013. Dynamic warping of seismic images, *Geophysics,* **78**(2), S105–S115.

Hefny, M., Zappone, A., Makhloufi, Y., de Haller, A. & Moscariello, A., 2020. A laboratory approach for the calibration of seismic data in the western part of the Swiss Molasse Basin: the case history of well Humilly-2 (France) in the Geneva area, *Swiss J. Geosci.,* **113,** doi:10.1186/s00015-020-00364-4.

Herraiz, M. & Espinosa, A.F., 1987. Coda waves: a review, *Pure appl. Geophys.,* **125,** 499–577.

Husen, S. & Kissling, E., 2001. Local earthquake tomography between rays and waves: fat ray tomography, *Phys. Earth planet. Inter.,* **125**(1–4), 171–191.

Islam, S.A., Powell, C.A. & Chapman, M.C., 2022. Velocity models for the crust hosting the main aftershock cluster of the 2011 Mineral, Virginia, Earthquake, *Seismol. Soc. Am.,* **93**(2A), 943–956.

Jiang, H., Zhan, H., Ma, Z. & Jiang, R., 2020. Comparative study of three-dimensional stress and crack imaging in concrete by application of inverse algorithms to coda wave measurements, *Sensors,* **20**(17), doi:10.3390/s20174899.

Johnson, P.A. *et al.*, 2013. Acoustic emission and microslip precursors to stick-slip failure in sheared granular material, *Geophys. Res. Lett.,* **40,** 5627–5631.

Johnson, P.A. *et al.*, 2021. Laboratory earthquake forecasting: a machine learning competition, *Proc. Natl. Acad. Sci.,* **118**(5), doi:10.1073/pnas.2011362118.

Kachanov, M., 1994. On the concept of damage in creep and in the brittle-elastic range, *Int. J. Damage Mech.,* **3**(4), 329–337.

Kang, P.K., Brown, S. & Juanes, R., 2016. Emergence of anomalous transport in stressed rough fractures, *Earth planet. Sci. Lett.,* **454,** 46–54.

Kaselow, A. & Shapiro, S.A., 2004. Stress sensitivity of elastic moduli and electrical resistivity in porous rocks, *J. geophys. Eng.,* **1**(1), doi:10.1088/1742-2132/1/1/001.

Kurz, J.H., Grosse, C.U. & Reinhardt, H.W., 2005. Strategies for reliable automatic onset time picking of acoustic emissions and of ultrasound signals in concrete, *Ultrasonics,* **43**(7), 538–546.

Latour, S., Schubnel, A., Nielsen, S., Madariaga, R. & Vinciguerra, S., 2013. Characterization of nucleation during laboratory earthquakes, *Geophys. Res. Lett.,* **40**(19), 5064–5069.

Livings, R., Dayal, V. & Barnard, D., 2016. Coda wave interferometry for the measurement of thermally induced ultrasonic velocity variations in CFRP laminates, *AIP Conf. Proc.,* **1706**(1), doi:10.1063/1.4940588.

Lockner, D.A., Byerlee, J.D., Kuksenko, V., Ponomarev, A. & Sidorin, A., 1991. Quasi-static fault growth and shear fracture energy in granite, *Nature,* **350**(6313), 39–42.

Main, I., Meredith, P. & Sammonds, P., 1992. Temporal variations in seismic event rate and b-values from stress corrosion constitutive laws, *Tectonophysics,* **211,** 233–246.

Marty, S., Schubnel, A., Bhat, H.S., Aubry, J., Fukuyama, E., Latour, S. & Madariaga, R., 2023. Nucleation of laboratory earthquakes: quantitative analysis and scalings, *J. geophys. Res.,* **128**(3), e2022JB026294, doi:10.1029/2022JB026294.

Marone, C., 1998. Laboratory-derived friction laws and their application to seismic faulting, *Ann. Rev. Earth planet. Sci.,* **26,** 643–696.

McLaskey, G.C., 2019. Earthquake initiation from laboratory observations and implications for foreshocks, *J. geophys. Res.,* **124**(12), 12 882–12 904.

McLaskey, G.C. & Kilgore, B.D., 2013. Foreshocks during the nucleation of stick-slip instability, *J. geophys. Res.,* **118**(6), 2982–2997.

Mignan, A., 2014. The debate on the prognostic value of earthquake foreshocks: a meta-analysis, *Nature,* **4,** doi:10.1038/srep04099.

Mikesell, T.D., Malcolm, A.E., Yang, D. & Haney, M.M., 2015. A comparison of methods to estimate seismic phase delays: numerical examples for coda wave interferometry, *J. geophys. Int.,* **202**(1), 347–360.

Müller, M., 2007. *Information Retrieval for Music and Motion,* Springer, 313pp.

Ohnaka, M., 1992. Earthquake source nucleation: A physical model for short-term precursors, *Tectonophysics,* **211**(1–4), 149–178.

Ohnaka, M., 2004. A constitutive scaling law for shear rupture that is inherently scale-dependent, and physical scaling of nucleation time to critical point, *Pure appl. Geophys.,* **161**(9–10), 1915–1929.

Ohnaka, M. & Shen, L., 1999. Scaling of the shear rupture process from nucleation to dynamic propagation: implications of geometric irregularity of the rupturing surfaces, *J. geophys. Res.,* **104**(B1), 817–844.

Paglialunga, F., Passelègue, F.X., Acosta, M. & Violay, M., 2021. Origin of the co-seismic variations of elastic properties in the crust: insight from the laboratory, *Geophys. Res. Lett.,* **48**(12), doi:10.1029/2021GL093619.

Passelègue, F.X., Brantut, N. & Mitchell, T.M., 2018. Fault reactivation by fluid injection: controls from stress state and injection rate, *Geophys. Res. Lett.,* **45**(23), 12–837.

Paterson, M.S. & Wong, T.F., 2005. *Experimental Rock Deformation—The Brittle Field,* pp. 59–111, Springer-Verlag.

Ratdomopurbo, A. & Poupinet, G., 1995. Monitoring a temporal change of seismic velocity in a volcano: application to the 1992 eruption of Mt. Merapi (Indonesia), *Geophys. Res. Lett.,* **22**(7), 775–778.

Rouet-Leduc, B., Hulbert, C., Lubbers, N., Barros, K., Humphreys, C.J. & Johnson, P.A., 2017. Machine learning predicts laboratory earthquakes, *Geophys. Res. Lett.,* **44**(18), 9276–9282.

Sakoe, H. & Chiba, S., 1978. Dynamic programming algorithm optimization for spoken word recognition, *IEEE Trans. Acoust., Speech, Signal Process.,* **26**(1), 43–49.

Scholz, C.H., 1968. Microfracturing and the inelastic deformation of rock in compression, *J. geophys. Res.,* **73**(4), 1417–1432.

Scuderi, M.M., Marone, C., Tinti, E., di Stefano, G. & Collettini, C., 2016. Precursory changes in seismic velocity for the spectrum of earthquake failure modes, *Nat. Geosci.,* **9**(9), 695–700.

Shreedharan, S., Bolton, D.C., Rivière, J. & Marone, C., 2021. Competition between preslip and deviatoric stress modulates precursors for laboratory earthquakes, *Earth planet. Sci. Lett.,* **553,** doi:10.1016/j.epsl.2020.116623.

Singh, J., Curtis, A., Zhao, Y., Cartwright-Taylor, A. & Main, I., 2019. Coda wave interferometry for accurate simultaneous monitoring of velocity and acoustic source locations in experimental rock physics, *J. geophys. Res.,* **124**(6), 5629–5655.

Snieder, R., 2006. The theory of coda wave interferometry, *Pure appl. Geophys.,* **163,** 455–473.

Snieder, R., Grêt, A., Douma, H. & Scales, J., 2002. Coda wave interferometry for estimating nonlinear behavior in seismic velocity, *Science,* **295**(5563), 2253–2255.

Soga, N., Mizutani, H., Spetzler, H. & Martin III, R.J., 1978. The effect of dilatancy on velocity anisotropy in Westerly granite, *J. geophys. Res.,* **83**(8), 4451–4458.

Stanchits, S., Vinciguerra, S. & Dresen, G., 2006. Ultrasonic velocities, acoustic emission characteristics and crack damage of basalt and granite, *Pure appl. Geophys.,* **163**(5–6), 974–993.

Stesky, R., 1978. Mechanisms of high temperature frictional sliding in Westerly granite, *Can. J. Earth Sci.,* **15**(5), 361–375.

Sugan, M., Kato, A., Miyake, H., Nakagawa, S. & Vuan, A., 2014. The preparatory phase of the 2009 Mw 6.3 L'Aquila earthquake by improving the detection capability of low-magnitude foreshocks, *Geophys. Res. Lett.,* **41**(17), 6137–6144.

Sun, S., Ji, S., Wang, Q., Xu, Z., Salisbury, M. & Long, C., 2012. Seismic velocities and anisotropy of core samples from the Chinese Continental Scientific Drilling borehole in the Sulu UHP terrane, eastern China, *J. geophys. Res.,* **117**(B1), doi:10.1029/2011JB008672.

Taira, T., Brenguier, F. & Kong, Q., 2015. Ambient noise-based monitoring of seismic velocity changes associated with the 2014 M w 6.0 South Napa earthquake, *Geophys. Res. Lett.,* **42,** 6997–7004.

Taira, T., Nayak, A., Brenguier, F. & Manga, M., 2018. Monitoring reservoir response to earthquakes and fluid extraction, Salton Sea geothermal field, California, *Sci. Adv.,* **4**(1), doi:10.1126/sciadv.1701536.

Taira, T., Silver, P.G., Niu, F. & Nadeau, R.M., 2008. Detecting seismogenic stress evolution and constraining fault zone rheology in the San Andreas Fault following the 2004 Parkfield earthquake, *J. geophys. Res.,* **113**(B3), doi:10.1029/2007JB005151.

Tape, C., Liu, Q., Maggi, A. & Tromp, J., 2009. Adjoint tomography of the southern California crust, *Science,* **325**(5943), 988–992.

Tape, C., West, M., Silwal, V. & Ruppert, N., 2013. Earthquake nucleation and triggering on an optimally oriented fault, *Earth planet. Sci. Lett.,* **363,** 231–241.

Taylor, G. & Hillers, G., 2020. Estimating temporal changes in seismic velocity using a Markov chain Monte Carlo approach, *J. geophys. Int.,* **220**(3), 1791–1803.

Thurber, C. & Ritsema, J., 2007. *Theory and Observations - Seismic Tomography and Inverse Methods,* pp. 323–360, Elsevier.

Trugman, D.T., McBrearty, I.W., Bolton, D.C., Guyer, R.A., Marone, C. & Johnson, P.A., 2020. The spatiotemporal evolution of granular microslip precursors to laboratory earthquakes, *Geophys. Res. Lett.,* **47**(16), doi:10.1029/2020GL088404.

Trugman, D.T. & Ross, Z.E., 2019. Pervasive foreshock activity across southern California, *Geophys. Res. Lett.,* **46**(15), 8772–8781.

Uchida, N. & Bürgmann, R., 2019. Repeating earthquakes, *Ann. Rev. Earth planet. Sci.,* **47,** 305–332.

Vidale, J.E. & Li, Y.G., 2003. Damage to the shallow Landers fault from the nearby Hector Mine earthquake, *Nature,* **421**(6922), 524–526.

Walsh, J.B., 1965. The effect of cracks on the uniaxial elastic compression of rocks, *J. geophys. Res.,* **70**(2), 399–411.

Wang, Q.Y., Campillo, M., Brenguier, F., Lecointre, A., Takeda, T. & Hashima, A., 2019. Evidence of changes of seismic properties in the entire crust beneath Japan after the Mw 9.0, 2011 Tohoku-oki earthquake, *J. geophys. Res.,* **124**(8), 8924–8941.

Watanabe, T. & Higuchi, A., 2015. Simultaneous measurements of elastic wave velocities and electrical conductivity in a brine-saturated granitic rock under confining pressures and their implication for interpretation of geophysical observations, *Prog. Earth planet. Sci.,* **2,** 1–12.

Wegler, U., Nakahara, H., Sens-Schönfelder, C., Korn, M. & Shiomi, K., 2009. Sudden drop of seismic velocity after the 2004 M w 6.6 mid-Niigata earthquake, Japan, observed with Passive Image Interferometry, *J. geophys. Res.,* **114,** doi:10.1029/2008JB005869.

Zhang, H. & Thurber, C.H., 2003. Development and applications of double-difference seismic tomography, *Bull. seism. Soc. Am.,* **93**(5), 1875–1889.

Zotz-Wilson, R., Boerrigter, T. & Barnhoorn, A., 2019. Coda-wave monitoring of continuously evolving material properties and the precursory detection of yielding, *J. acoust. Soc. Am.,* **145**(2), 1060–1068.